



## OPEN ACCESS

EDITED BY  
Zhanwu Lu,  
Chinese Academy of Geological Sciences,  
China

REVIEWED BY  
Sanzhong Li,  
Ocean University of China, China  
Ming Chen,  
China University of Geosciences Wuhan,  
China

\*CORRESPONDENCE  
Rui Gao,  
✉ gaorui66@mail.sysu.edu.cn  
Jia-Qi Liu,  
✉ liujq@mail.iggcas.ac.cn

SPECIALTY SECTION  
This article was submitted to Structural  
Geology and Tectonics,  
a section of the journal  
Frontiers in Earth Science

RECEIVED 06 November 2022  
ACCEPTED 16 January 2023  
PUBLISHED 30 January 2023

CITATION  
Chen S-S, Wu D-Y, Gao R, Cheng Q and  
Liu J-Q (2023), *In-situ* Sr isotope  
disequilibrium in plagioclases from Late  
Cenozoic basalts in Leiqiong area:  
Evidence for the role of the Hainan plume  
and mantle metasomatism due to a paleo-  
subduction event.  
*Front. Earth Sci.* 11:1090803.  
doi: 10.3389/feart.2023.1090803

COPYRIGHT  
© 2023 Chen, Wu, Gao, Cheng and Liu.  
This is an open-access article distributed  
under the terms of the [Creative Commons  
Attribution License \(CC BY\)](https://creativecommons.org/licenses/by/4.0/). The use,  
distribution or reproduction in other  
forums is permitted, provided the original  
author(s) and the copyright owner(s) are  
credited and that the original publication in  
this journal is cited, in accordance with  
accepted academic practice. No use,  
distribution or reproduction is permitted  
which does not comply with these terms.

# *In-situ* Sr isotope disequilibrium in plagioclases from Late Cenozoic basalts in Leiqiong area: Evidence for the role of the Hainan plume and mantle metasomatism due to a paleo-subduction event

Shuang-Shuang Chen<sup>1,2,3,4</sup>, Duo-Yang Wu<sup>1,2,3</sup>, Rui Gao<sup>1,2,5\*</sup>,  
Qiuming Cheng<sup>1,2</sup> and Jia-Qi Liu<sup>6\*</sup>

<sup>1</sup>School of Earth Sciences and Engineering, Sun Yat-sen University, Guangzhou, China, <sup>2</sup>Southern Marine Science and Engineering Guangdong Laboratory (Zhuhai), Zhuhai, China, <sup>3</sup>Guangdong Provincial Key Lab of Geological Processes and Mineral Resources, Guangzhou, China, <sup>4</sup>State Key Laboratory of Marine Environmental Science, Xiamen University, Xiamen, China, <sup>5</sup>State Key Laboratory of Tibetan Plateau Earth System, Environment and Resources (TPESER), Institute of Tibetan Plateau Research, Chinese Academy of Sciences, Beijing, China, <sup>6</sup>Key Laboratory of Cenozoic Geology and Environment, Institute of Geology and Geophysics, Chinese Academy of Sciences, Beijing, China

The origin of the EM2 (enriched mantle 2)-type reservoir beneath the Southeast Asia is controversial. In this study, we present new *in-situ* major and trace element (olivine, clinopyroxene, and plagioclase), and Sr isotopic compositions (plagioclase) for Leiqiong basaltic rocks to explain the potential source of Leiqiong EM2-like reservoir. Leiqiong olivines show the normal zoning textures with *in-situ* trace element heterogeneity, Leiqiong plagioclases exhibit the complex zoning textures with *in-situ* <sup>87</sup>Sr/<sup>86</sup>Sr isotopic disequilibria. It likely suggests the contribution to an individual crystal by the incorporation of heterogeneous components. The olivine and plagioclase phenocrysts, and the calculated Leiqiong clinopyroxene-equilibrium melts show the features of OIB-type enriched compositions associated with the plume, likely indicating the presence of Hainan mantle plume. The clear disequilibrium of <sup>87</sup>Sr/<sup>86</sup>Sr isotopic ratios among bulk-rock, plagioclase phenocryst, and groundmass likely indicates the isotopically heterogeneous mantle source and the influence of the recycled subduction-related H<sub>2</sub>O-enriched oceanic fluid/melts carried by the deep Hainan plume. Leiqiong olivines are crystallized by the incorporation of pyroxenitic mantle source, but different from those from olivine-rich peridotitic mantle lithology, likely due to the reaction between eclogite-derived silicate melts (recycled oceanic crust) and peridotite.

## KEYWORDS

plagioclase, *in situ* Sr isotope disequilibrium, Late Cenozoic basalts, Hainan mantle plume, Leiqiong area

## 1 Introduction

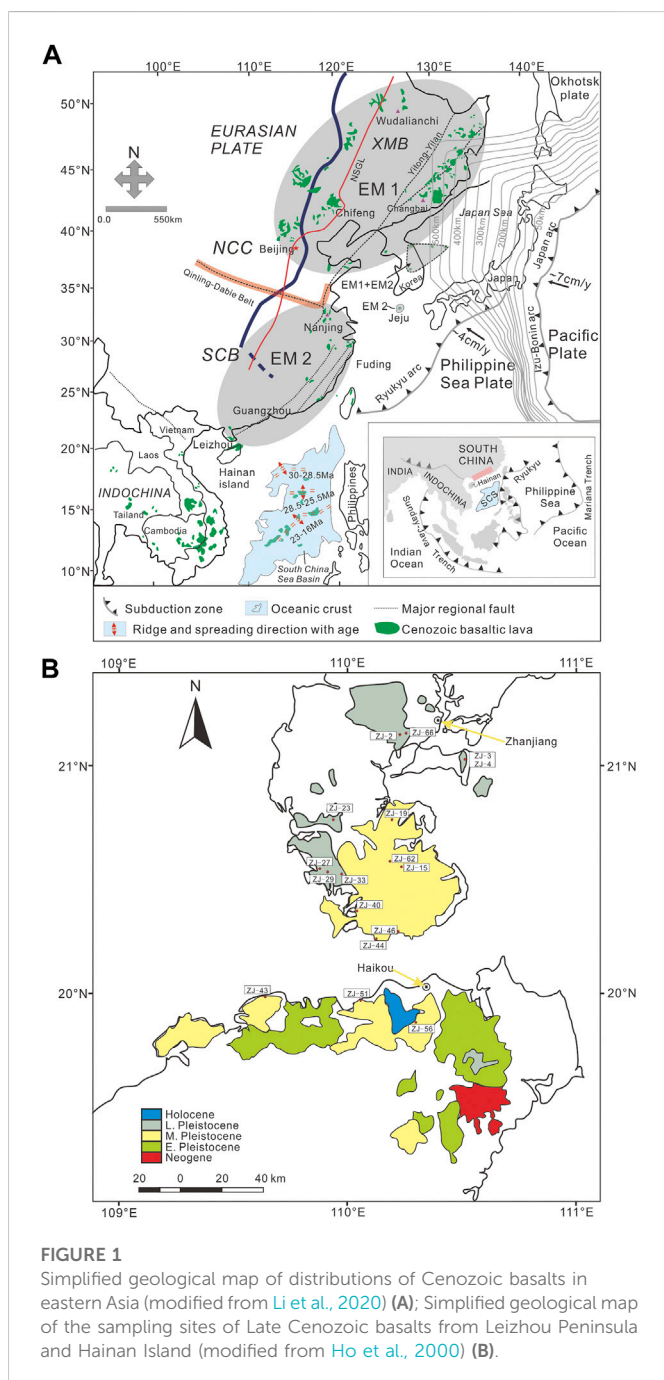
Late Cenozoic basaltic volcanism is widely distributed along East China, from the north of Heilongjiang province to the south of Hainan Island and South China Sea (SCS) (Lee et al., 2021), which belongs to parts of the circum Pacific volcanic belt (Figure 1A). The Northeast China Cenozoic basalts have an EM1 (enriched mantle 1)-type Ocean Island

Basalt (OIB) isotopic affinity (Figure 1A), likely attributed to the incorporation of ancient sediments from the stagnant subducted paleo-Pacific plate in the mantle transition zone (Huang and Zhao, 2006; Li and Van der Hilst, 2010; Li et al., 2015; 2016; Xu et al., 2018) and the lithospheric thinning of the North China Craton (Xu, 2001; Gao et al., 2002; Ma et al., 2014). The Southeast China and Jeju Island Cenozoic basalts have an EM2 (enriched mantle 2)-type OIB isotopic affinity (Figure 1A), likely due to the presence of the Hainan plume extending to 660 km depth (Zou et al., 2000; Lebedev and Nolet, 2003; Chen et al., 2009; Brenna et al., 2012a; 2012b), even to 1,300 km depth (Huang and Zhao, 2006) and 1,900 km depth (Montelli et al., 2006) beneath the Leiqiong Peninsula. The excess mantle temperature (Wei and Chen, 2016), the Holocene volcanic extrusion rate (Liu et al., 2015; Li et al., 2020), the geochemical

features (Yan et al., 2018; Yu et al., 2018; Zhang et al., 2018), and the low-velocity seismic structure (Huang and Zhao, 2006; Montelli et al., 2006; Brenna et al., 2012a; 2012b) collectively testify the crucial role of Hainan plume in the extensive volcanic activities beneath the SE Asia. However, apart from the above-mentioned Hainan plume, there is still controversy about the origin of the EM2-type reservoir beneath the SE Asia, such as the proposed asthenosphere mantle origin (Choi et al., 2006), the delaminated lithospheric mantle (Zou and Fan, 2010), the presence of a sialic crustal component or a slab-derived component (Tu et al., 1991; Qiu et al., 2019), the subducted pelagic sediments (Wang and Zhang, 2022), and the thermally metasomatized continental lithospheric mantle (Zhou and Mukasa, 1997; Ho et al., 2003; Hoàng et al., 2013; Qiu et al., 2019).

Massive Late Cenozoic intraplate magmatism in the Zhejiang–Fujian–Leiqiong area occurred following cessation of South China Sea seafloor spreading (<16 Ma) (Ho et al., 2003), likely due to the gradually westward and northward migration of the South China Sea mid-ocean ridge system and the collision of the Eurasia continent with the Luzon arc since mid-Miocene (Chung et al., 1994; Ho et al., 2003). Ho et al. (2003) took advantage of Sr–Nd–Pb isotopic compositions of Zhejiang–Fujian Late Cenozoic basalts to prove the presence of the continental lithospheric mantle, which are likely attributed to mantle metasomatism due to a paleo-subduction event (Hoàng et al., 2013; Qiu et al., 2019). In addition, massive studies on the eastern Asia Cenozoic basalts (e.g., Chen et al., 2009; Zhang et al., 2009; Zhang and Guo, 2016) and Mesozoic basalts (e.g., Jia et al., 2020) have proven the influence of recycled oceanic crustal components derived from the paleo-subduction Pacific plate (Kuritani et al., 2011; Liu et al., 2016; Chen et al., 2017; Xu et al., 2018; Yu et al., 2019). The Pacific plate westward subducted beneath the eastern Asia since the Mesozoic (Zeng et al., 2016; Sun et al., 2018). Consequently, the components of the involved recycled crustal material originated from a stagnant Pacific plate in the mantle transition zone were continuously supplied to the Mesozoic and Cenozoic eastern Asia mantle source (Meng et al., 2012; Tang et al., 2013; Zeng et al., 2016; Sun et al., 2018; Qiu et al., 2019; Jia et al., 2020).

The bulk-rock isotopic compositions of Leiqiong Late Cenozoic basalts have revealed contributions from a wide variety of source components, including Hainan plume (Montelli et al., 2006; Zou and Fan, 2010; Wang et al., 2012; Lee et al., 2021), enriched metasomatized continental lithospheric mantle source (Ho et al., 2003; Hoàng et al., 2013), recycled oceanic components (Wang et al., 2012; Jin et al., 2020; Lee et al., 2021), and crustal contamination (Tu et al., 1991). However, no relevant studies have been found to be focused on the mineral-scale and small-spatial-scale variations within the mineral and groundmass phases. It is undeniable that the bulk-rock geochemical and isotopic compositions can efficiently carry out the mantle source interpretations. However, the bulk-rocks consist of a variety of materials, and represent the sum of all the components and petrogenetic processes that have contributed to it (Ramos et al., 2005). Furthermore, the bulk-rock geochemical features are easily altered by melt aggregation and magma mixing (Feineman et al., 2013; Rasmussen et al., 2020). Thus, the mineral-scale magma heterogeneity, the initial mantle-derived features, the shallow-level crustal contributions, and the fine-scale melt



aggregation are best explained by utilizing the micro-trace-element and micro-isotope analyses within the individual phenocrysts (Bryce and DePaolo, 2004; Davidson et al., 2005; Ramos et al., 2005; Ramos and Reid, 2005; Rasmussen et al., 2020). The studied Leiqiong Pleistocene basalts contain large amounts of plagioclase, clinopyroxene, and olivine phenocrysts, and plagioclase groundmass, which are distinguished by relatively high and useful trace-element and Sr isotope contents due to relatively slow diffusion rates of these elements (Lange et al., 2013). Here we present the *in-situ* geochemistry and Sr isotope variations in phenocrysts and groundmass of Leiqiong Pleistocene basalts to 1) constrain the role of the Hainan plume and mantle metasomatism due to a paleo-subduction event; 2) gain insight into the mantle geochemical heterogeneity beneath the Leiqiong Area; 3) determine the potential source materials of Leiqiong EM2-like reservoir.

## 2 Geological setting and sample description

Late Cenozoic basaltic lava flows in Hainan Island and the Leizhou Peninsula belong to the largest area of basalts in South China with exposures of over 7,000 km<sup>2</sup> (Ho et al., 2000; Yu et al., 2003; Zou and Fan, 2010; Figure 1). They are located at the southernmost portion of the South China block and the

northern edge of the SCS Basin (Figure 1; Lee et al., 2021), which belong to the East Asiatic continental margin and the circum-Pacific volcanic belt (Figure 1). Leizhou Peninsula is situated at the southernmost portion of mainland China with a relatively flat volcanic topography with average 10–50 m altitude (Lee et al., 2021). Late Cenozoic volcanic activities in the Leiqiong area are widespread during the following four volcanism stages, including the Pliocene ( $5.6 \pm 3.8$  Ma), early Pleistocene ( $2.0 \pm 0.8$  Ma), middle-late Pleistocene ( $0.7 \pm 0.1$  Ma), and Holocene volcanism, respectively (Zhou et al., 1988; Ho et al., 2000; Liu et al., 2015). The early volcanic stage (Pliocene and early Pleistocene) mainly consists of quartz tholeiites and olivine tholeiites, whereas the later stage (middle-late Pleistocene and Holocene) produced mostly alkali olivine basalts and olivine tholeiites (Fan and Menzies, 1992).

Seventeen Middle and Late Pleistocene volcanic rocks recovered from Leiqiong area mainly belong to alkali olivine basalts and olivine tholeiites, which are presented in detail in the Supplementary Table S1. These Leiqiong basalts occur as grayish black lava flows with a compact and massive block and a porphyritic texture (Figure 2), they do not belong to cumulates with clear cumulus textures. Late Pleistocene Leiqiong basalts (ZJ-2, ZJ-4, ZJ-27, ZJ-33, and ZJ-66) contain large amounts of large hexagonal olivine phenocrysts (50 vol%; 0.2–0.8 mm; Figures 2A, B), large automorphic tabular plagioclase with a remarkable oscillatory zoning texture (15 vol%; 0.2–0.6 mm; Figure 2C),

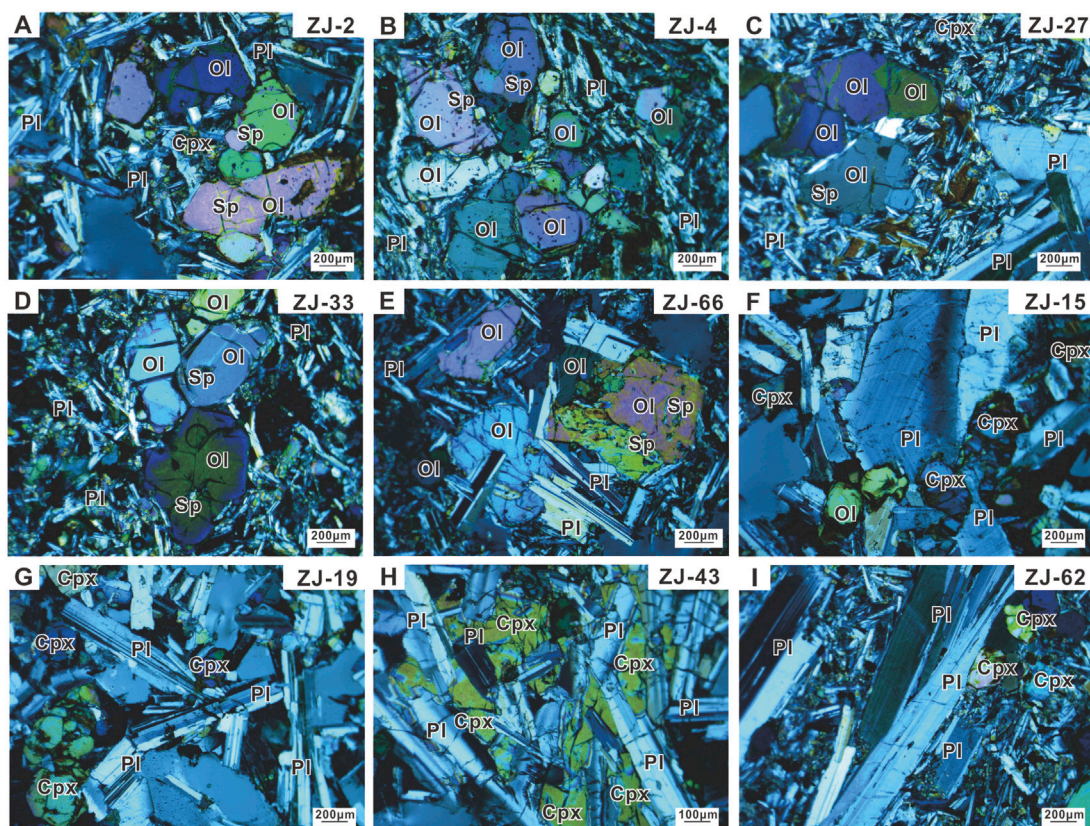
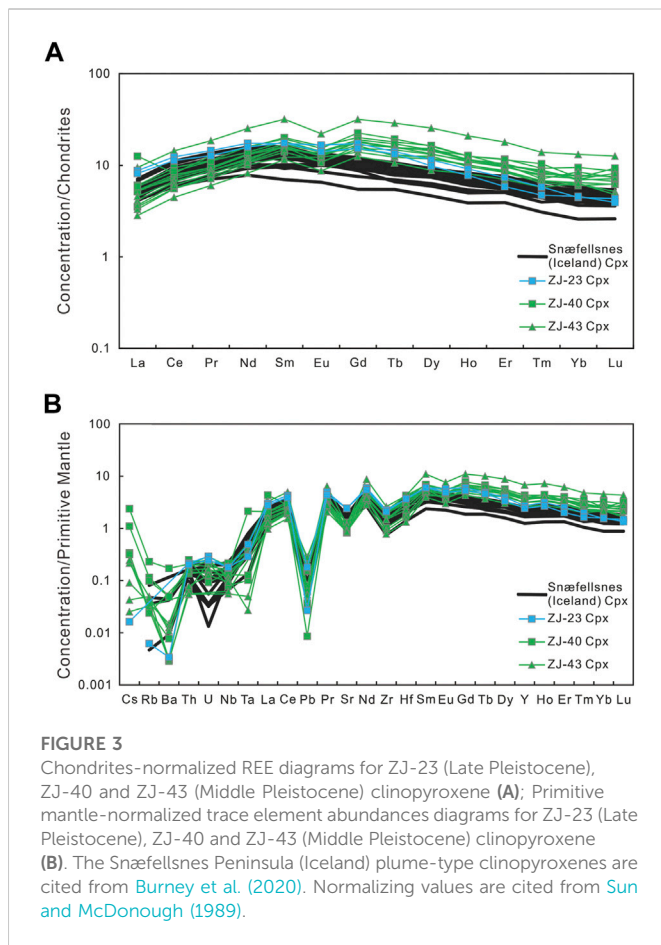


FIGURE 2

Optical microscope images of ZJ-2 (A), ZJ-4 (B), ZJ-27 (C), ZJ-33 (D), ZJ-66 (E) from Late Pleistocene Leiqiong basalts; ZJ-15 (F), ZJ-19 (G), ZJ-43 (H), ZJ-62 (I) from Middle Pleistocene Leiqiong basalts. Ol, olivine; Cpx, clinopyroxene; Pl, plagioclase; Sp, spinel.



**FIGURE 3**  
Chondrites-normalized REE diagrams for ZJ-23 (Late Pleistocene), ZJ-40 and ZJ-43 (Middle Pleistocene) clinopyroxene (A); Primitive mantle-normalized trace element abundances diagrams for ZJ-23 (Late Pleistocene), ZJ-40 and ZJ-43 (Middle Pleistocene) clinopyroxene (B). The Snæfellsnes Peninsula (Iceland) plume-type clinopyroxenes are cited from Burney et al. (2020). Normalizing values are cited from Sun and McDonough (1989).

small needle-like plagioclase phenocrysts (20 vol%; 0.05–0.4 mm; Figure 2E), and few irregularly-shaped clinopyroxene (15 vol%; 0.05–0.2 mm; Figures 2A–C). The olivine minerals do not belong to xenocrysts because these olivines do not exhibit the erosion edges (Figures 2A, B). These large well-shaped olivines show a normal zoning texture (Figure 2D) and contain several spinel inclusions (Figures 2A–E). The groundmass mainly contains fine needle-shaped plagioclase, some altered dark-colored mineral particles, and volcanic glass. In comparison, Middle Pleistocene Leiqiong basalts (ZJ-15, ZJ-19, ZJ-43, and ZJ-62) have remarkably less and smaller olivine phenocrysts (15 vol%; 0.05–0.2 mm; Figure 2F) and more clinopyroxene (30 vol%; 0.1–0.6 mm; Figure 2H) and plagioclase phenocrysts (50 vol%; 0.2–1.0 mm; Figures 2F–I). Massive large plagioclases exhibit complex zoning textures including an oscillatory zoning (Figure 2F) and a normal zoning texture (Figures 2H, I). The groundmass mainly consists of fine needle-shaped plagioclase, small broken altered irregularly-shaped clinopyroxene, olivine, Fe±Ti oxide mineral and glassy materials (Figure 2).

### 3 Analytical methods

Major element and trace element analyses of olivines, clinopyroxenes, and plagioclases were conducted using an Agilent 7700e Laser-ablation Inductively Coupled Plasma Mass Spectrometer (LA-ICP-MS) at the Wuhan SampleSolution Analytical Technology Co., Ltd., Wuhan, China. Detailed operating conditions for the laser

ablation system and the ICP-MS instrument and data reduction are the same as description by Zong et al. (2017). Laser sampling was performed using a GeoLas HD laser ablation system that consists of a COMPexPro 102 ArF excimer laser (wavelength of 193 nm and maximum energy of 200 mJ) and a MicroLas optical system. An Agilent 7700e ICP-MS instrument was used to acquire ion-signal intensities. The spot size and frequency of the laser were set to 44  $\mu\text{m}$  and 5 Hz, respectively. Each analysis incorporated a background acquisition of approximately 20–30 s followed by 50 s of data acquisition from the sample. The internal standard used was  $^{29}\text{Si}$  determined by EPMA analysis. Three geochemically distinct reference glasses (BCR-2G, BIR-1G, BHVO-2G) were used to cover the possible geochemical spectrum. An Excel-based software ICPMSDataCal10.8 was used to perform off-line selection and integration of background and analyzed signals, time-drift correction and quantitative calibration for trace element analysis (Liu et al., 2008). Relative standard deviations (% RSD) of LA-ICP-MS analyses are less than 20% for all trace elements. The major and trace element compositions of olivines, clinopyroxenes, plagioclases are presented in Supplementary Tables S2–S4. The trace element values of standard samples during the mineral analyzing process are presented in Supplementary Table S5.

Sr isotope ratios of feldspars were measured by a Neptune Plus MC-ICP-MS (Thermo Fisher Scientific, Bremen, Germany) in combination with a Geolas HD excimer ArF laser ablation system (Coherent, Göttingen, Germany) at the Wuhan Sample Solution Analytical Technology Co., Ltd, Hubei, China. The Neptune Plus was equipped with nine Faraday cups fitted with  $10^{11} \Omega$  resistors. The Faraday collector configuration of the mass system was composed of an array from L4 to H3 to monitor Kr, Rb, Er, Yb and Sr. The combination of the high-sensitivity X-skimmer cone and Jet-sample cone was employed. In the laser ablation system, helium was used as the carrier gas for the ablation cell. For a single laser spot ablation, the spot diameter ranged from 60 to 160  $\mu\text{m}$  dependent on Sr signal intensity. The pulse frequency was from 8 to 15 Hz, but the laser fluence was kept constant at  $\sim 10 \text{ J}/\text{cm}^2$ . A new signal smoothing device (Hu et al., 2015) was used downstream from the sample cell to eliminate the short-term variation of the signal. All data reduction for the MC-ICP-MS analysis of Sr isotope ratios was conducted using “Iso-Compass” software (Zhang et al., 2020). The interference correction strategy was the same as the one reported by Zhang et al. (2018). Firstly, the regions of integration for both gas background and sample were selected. Following background correction, which removes the background  $\text{Kr}^+$  signals, no additional Kr peak stripping was applied. Interferences were corrected in the following sequence: 1) the interferences of  $^{168}\text{Er}^{++}$  on  $^{84}\text{Sr}$ ,  $^{170}\text{Er}^{++}$  and  $^{170}\text{Yb}^{++}$  on  $^{85}\text{Rb}$ ,  $^{172}\text{Yb}^{++}$  on  $^{86}\text{Sr}$ , and  $^{174}\text{Yb}^{++}$  on  $^{87}\text{Sr}$  were corrected based on the measured signal intensities of  $^{167}\text{Er}^{++}$ ,  $^{173}\text{Yb}^{++}$  and the natural isotope ratios of Er and Yb (Berglund and Wieser, 2011); 2) the isobaric interference of  $^{87}\text{Rb}$  on  $^{87}\text{Sr}$  was corrected by monitoring the  $^{85}\text{Rb}$  signal intensity and a user-specified  $^{87}\text{Rb}/^{85}\text{Rb}$  ratio using an exponential law for mass bias. The user-specified  $^{87}\text{Rb}/^{85}\text{Rb}$  ratio was calculated by measuring some reference materials with a known  $^{87}\text{Sr}/^{86}\text{Sr}$  ratio. Following the interference corrections, mass fractionation of Sr isotopes was corrected by assuming  $^{88}\text{Sr}/^{86}\text{Sr} = 8.375,209$  (Zhang et al., 2018) and applying the exponential law. Two natural feldspar megacrysts, YG0440 (albite) and YG4301 (anorthite) were used as the unknown samples to verify the accuracy of the calibration method

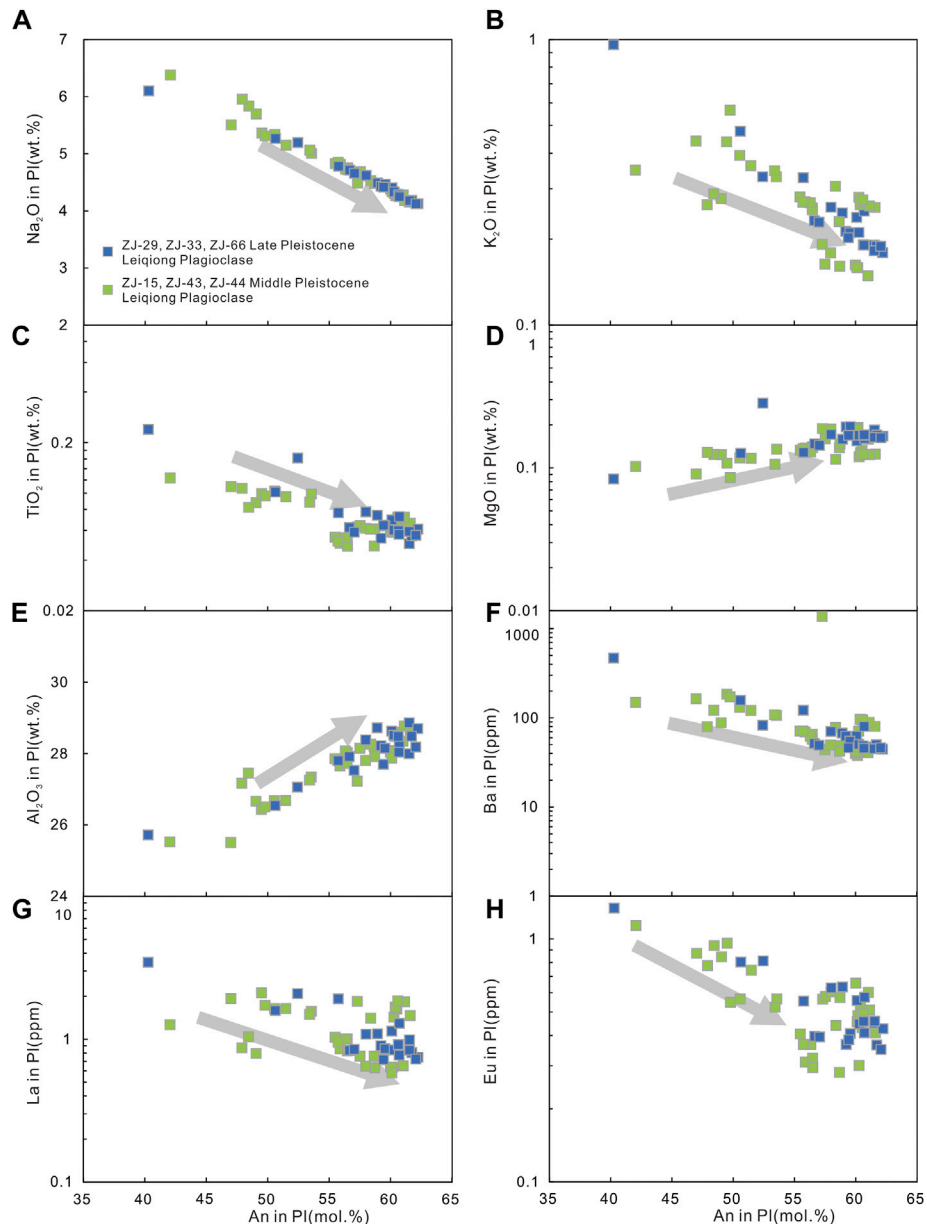


**FIGURE 4**

$\text{Na}_2\text{O}$  (wt%) versus An (mol%) (A);  $\text{K}_2\text{O}$  (wt%) versus An (mol%) (B);  $\text{TiO}_2$  (wt%) versus An (mol%) (C);  $\text{MgO}$  (wt%) versus An (mol%) (D);  $\text{Al}_2\text{O}_3$  (wt%) versus An (mol%) (E); Ba (ppm) versus An (mol%) (F); La (ppm) versus An (mol%) (G); Eu (ppm) versus An (mol%) (H) for Middle (ZJ-15; ZJ-43; ZJ-44) and Late (ZJ-29; ZJ-33; ZJ-66) Pleistocene Leiqiong plagioclases.

for *in situ* Sr isotope analysis of feldspars. The chemical and Sr isotopic compositions of YG0440 and YG4301 have been reported by Zhang et al. (2018). The Sr isotopic ratios of Sites 907, 913, and 911 plagioclase phenocrysts are presented in Supplementary Table S6.

## 4 Results

### 4.1 Olivine

Our analyzed olivine minerals do not belong to xenocrysts because these olivines do not exhibit the erosion edges (Figures

2A, B). Massive hexagonal olivine phenocrysts with some spinel inclusions are observed from Late Pleistocene Leiqiong basalts (Figures 2A–E). ZJ-2, ZJ-29, ZJ-33, and ZJ-66 (Late Pleistocene) olivines have Fo contents of 74.19–83.80, CaO values of 0.19–0.30 wt%, NiO values of 0.14–0.33 wt%, and MnO values of 0.18–0.28 wt% (Supplementary Table S2). These Late Pleistocene olivines (ZJ-2, ZJ-29, ZJ-33, and ZJ-66) exhibit significantly normal zoning textures (Supplementary Figures S2, S3) with higher Fo contents in the core (77.97–83.48; 79.12–83.80; 79.58–83.65; 78.77–83.47) and relatively lower Fo contents in the rim (74.19–77.84; 75.57–79.55; 78.28–81.95; 74.97–78.29; Supplementary Table S2; Supplementary Figures S2, S3). In comparison, less and smaller

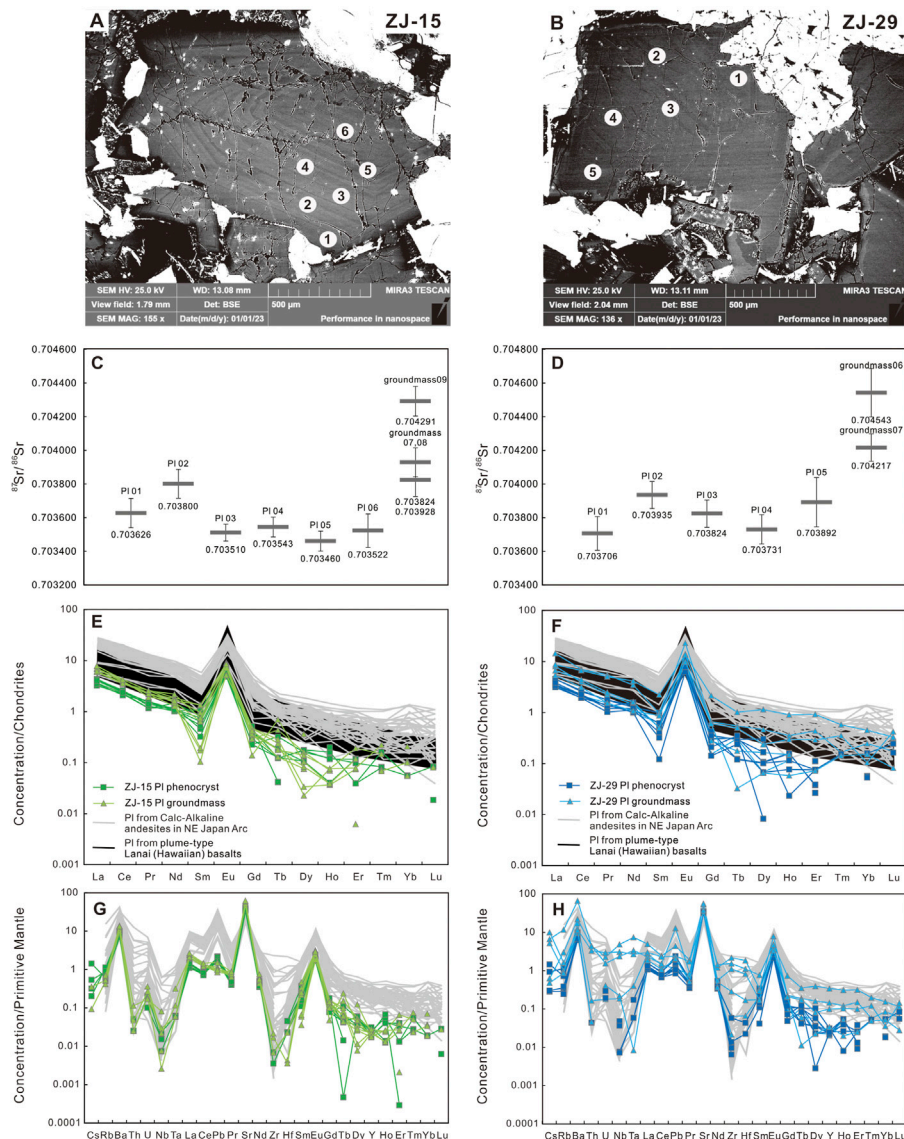


**FIGURE 5**

Optical microscope images of plagioclase from ZJ-15 (A) and ZJ-29 (B). The variation in Sr isotope composition (gray square) for ZJ-15 plagioclase phenocrysts and groundmass (C), ZJ-29 plagioclase phenocrysts and groundmass (D). Chondrites-normalized REE diagrams for ZJ-15 plagioclase phenocrysts and groundmass (E), ZJ-29 plagioclase phenocrysts and groundmass (F). Primitive mantle-normalized trace element abundances diagrams from ZJ-15 plagioclase phenocrysts and groundmass (G), ZJ-29 plagioclase phenocrysts and groundmass (H). Black lines represent the plagioclase data from the plume-type Lanai (Hawaiian) basalts (West et al., 1992). French grey lines represent the plagioclase data from the mantle-derived Medium-K Calc-Alkaline andesites in NE Japan Arc (Takahashi et al., 2012). Normalizing values are cited from Sun and McDonough (1989).

olivine phenocrysts are observed from Middle Pleistocene Leiqiong basalts (Figures 2F–I). ZJ-19, ZJ-51, ZJ-56, and ZJ-62 (Middle Pleistocene) olivines have relatively lower Fo (57.23–83.98), Cr (27.7–739 ppm), and Ni contents (720–2,684 ppm), and higher CaO (0.19–1.39 wt%) and MnO (0.19–0.44 wt%) contents (Supplementary Figure S1; Supplementary Table S2) compared to those of Late Pleistocene olivines. Leiqiong olivines show the positive correlations between  $\text{Al}_2\text{O}_3$ , Cr, Ni and Fo contents (Supplementary Figure S1A, E–F), the negative correlations between CaO, MnO, Ti, Y, Yb and Fo values (Supplementary Figure S1B–D, G–H). These olivines have clearly higher CaO (0.19–1.39 wt%) and MnO (0.18–0.44 wt%) contents compared to those of olivines in mantle xenoliths (CaO < 0.1 wt%; MnO < 0.15 wt

%), suggesting these olivines are not mantle-derived xenocrysts but crystallize from a magma system (Thompson and Gibson, 2000; Ren et al., 2004). Drouin et al. (2009) have pointed out that the trace element compositions of olivines in basaltic rock samples are difficult to detect. The description of *in-situ* olivine trace elements is presented in the Supplementary I.

## 4.2 Clinopyroxene

More and larger pyroxene phenocrysts are found from Middle Pleistocene Leiqiong basalts (ZJ-40; ZJ-43; Figure 2H) relative to those of Late Pleistocene Leiqiong basalts (ZJ-23). ZJ-23, ZJ-40,

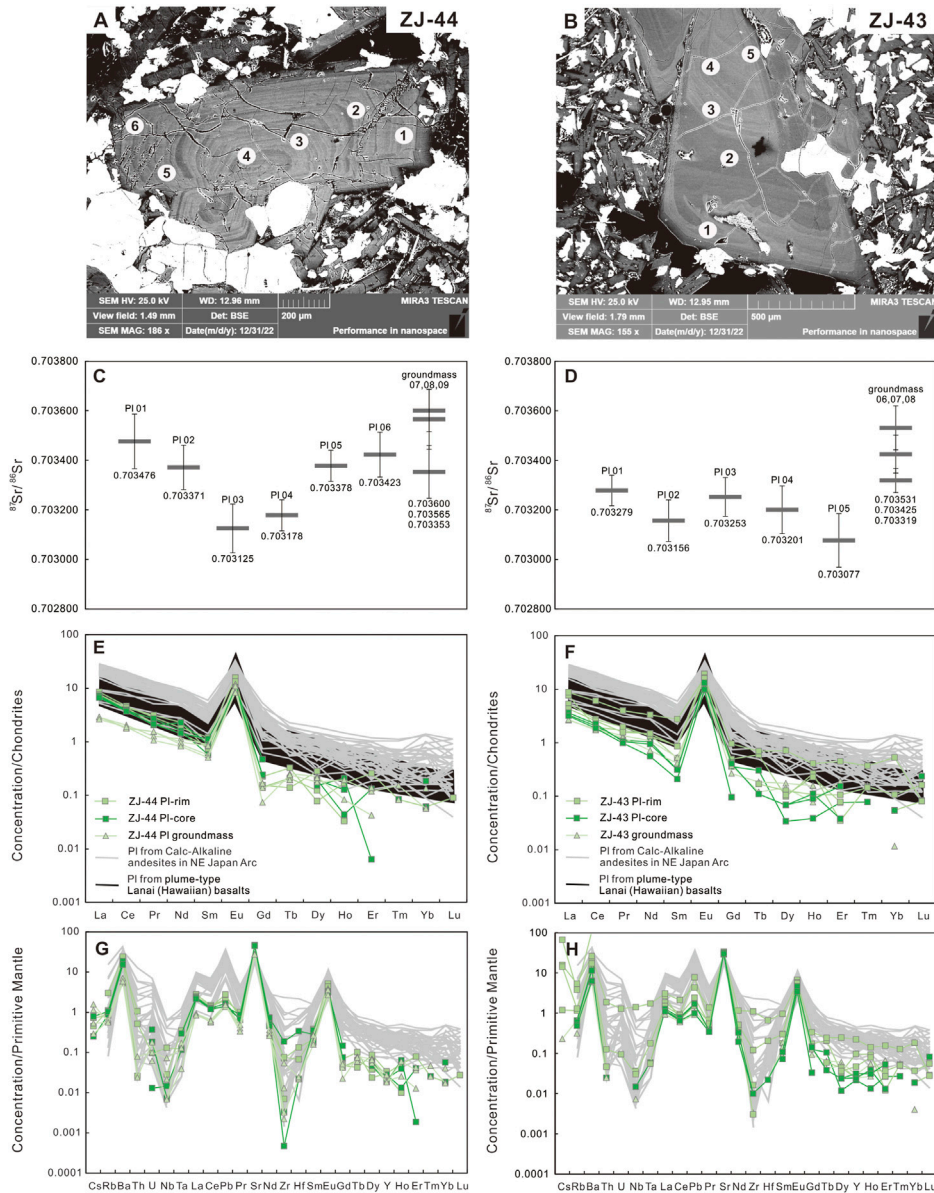


**FIGURE 6**

Optical microscope images of plagioclase from ZJ-44 (A) and ZJ-43 (B). The variation in Sr isotope composition (gray square) for ZJ-44 plagioclase cores, rims, and groundmass (C), ZJ-43 plagioclase cores, rims, and groundmass (D). Chondrites-normalized REE diagrams for ZJ-44 plagioclase cores, rims, and groundmass (E), ZJ-43 plagioclase cores, rims, and groundmass (F). Primitive mantle-normalized trace element abundances diagrams for ZJ-44 plagioclase cores, rims, and groundmass (G), ZJ-43 plagioclase cores, rims, and groundmass (H). Black lines represent the plagioclase data from the plume-type Lanai (Hawaiian) basalts (West et al., 1992). French grey lines represent the plagioclase data from the mantle-derived Medium-K Calc-Alkaline andesites in NE Japan Arc (Takahashi et al., 2012). Normalizing values are cited from Sun and McDonough (1989).

and ZJ-43 pyroxenes mainly belong to augite with the compositions of  $Wo_{35.0-43.4}En_{42.5-47.6}Fs_{10.5-19.3}$  (Supplementary Table S3; Supplementary Figure S5). ZJ-23 (Late Pleistocene) clinopyroxenes have significantly higher CaO (21.29–21.56 wt%) and Mg# (70.4–71.5) values, much lower MnO (0.15–0.16 wt%), Co (41.6–42.2 ppm), Yb (0.76–0.78 ppm), and Y (11.1–12.3 ppm) contents compared to those of ZJ-40 and ZJ-43 (Middle Pleistocene) clinopyroxenes (CaO=17.41–20.16 wt%; Mg#=55.9–66.7; MnO=0.19–0.27 wt%; Co=48.2–56.3 ppm; Yb=1.02–2.23 ppm; Y=11.9–30.7 ppm; Supplementary Figure S6;

Supplementary Table S3). ZJ-23, ZJ-40, and ZJ-43 clinopyroxenes display the positive correlations between CaO, Cr, Ni and Mg# values (Supplementary Figure S6B–D), the negative correlations between MnO, Ti, Co, Yb, Y and Mg# (Supplementary Figure S6A, E–H).

Middle (ZJ-40; ZJ-43) and Late (ZJ-23) Pleistocene Leiqiong clinopyroxenes did not show significant differences in compositions. ZJ-23, ZJ-40, and ZJ-43 clinopyroxenes show the slight depletion of LREE ( $La_N=2.83-12.6$  ppm) and HREE ( $Yb_N=4.45-13.1$  ppm), the relative enrichment of Middle REE

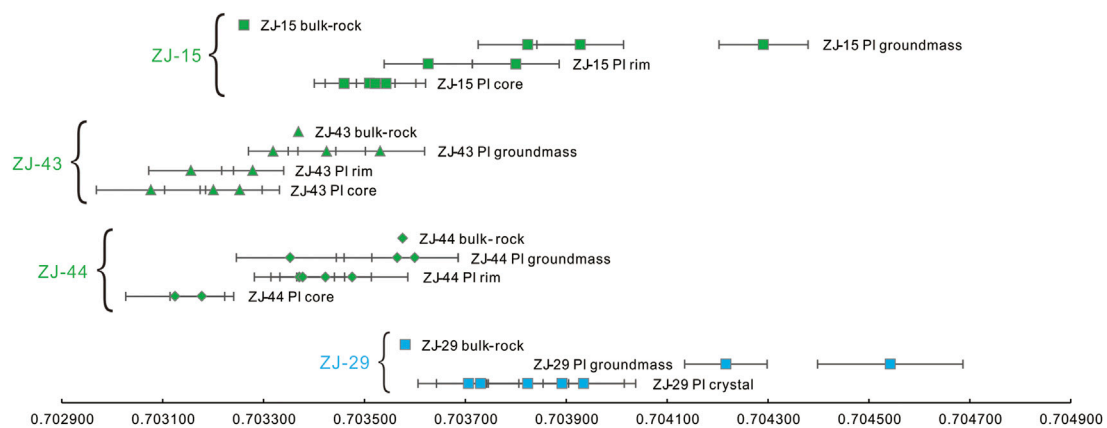


**FIGURE 7**

The *in-situ* Sr isotopes of plagioclase phenocrysts and plagioclase groundmass from ZJ-15, ZJ-43, and ZJ-44 (Middle Pleistocene) Leiqiong basalts and ZJ-29 (Late Pleistocene) Leiqiong basalts. ZJ-15, ZJ-43, and ZJ-44 (Middle Pleistocene) Leiqiong bulk-rock data are from Han et al. (2009). ZJ-29 (Late Pleistocene) Leiqiong bulk-rock data are from Zhu and Wang (1989).

(MREE;  $\text{Sm}_N=11.5\text{--}31.9$  ppm;  $\text{Gd}_N=12.5\text{--}31.8$  ppm), the slightly flat REE patterns ( $\text{La}/\text{Yb}_N=0.45\text{--}1.97$ ;  $\text{Gd}/\text{Yb}_N=1.97\text{--}3.89$ ), and the slightly Eu negative anomalies ( $\delta\text{Eu}=0.66\text{--}0.96$ ; Figure 3). In addition, these clinopyroxenes exhibit the significant Pb negative anomalies relative to Ce ( $\text{Pb}/\text{Ce}_{\text{PM}}=0.00\text{--}0.14$ ), the depletion of Sr and Zr relative to Nd and Hf ( $\text{Sr}/\text{Nd}_{\text{PM}}=0.14\text{--}0.44$ ;  $\text{Zr}/\text{Hf}_{\text{PM}}=0.48\text{--}0.65$ ), and the negative anomalies of Ba relative to Rb ( $\text{Ba}/\text{Rb}_{\text{PM}}=0.06\text{--}0.75$ ; Figure 3).

### 4.3 Plagioclase

Late Pleistocene Leiqiong feldspars (ZJ-29; ZJ-33; ZJ-66) belong to labradorite with the compositions of  $\text{Ab}_{36.7\text{--}53.9}\text{An}_{40.3\text{--}62.2}\text{Or}_{1.05\text{--}5.81}$  (Supplementary Table S4), whereas Middle Pleistocene Leiqiong feldspars (ZJ-15; ZJ-43; ZJ-44) are mainly andesine and labradorite with the compositions of  $\text{Ab}_{36.9\text{--}55.9}\text{An}_{42.1\text{--}61.6}\text{Or}_{0.88\text{--}3.26}$  (Supplementary Table S4). Comparatively speaking, Late Pleistocene Leiqiong feldspars have slightly higher An (40.3–62.2 mol%), MgO (0.08–0.28 wt%),  $\text{Al}_2\text{O}_3$  (25.72–28.86 wt%) contents, relatively lower  $\text{Na}_2\text{O}$  (4.13–6.10 wt%) contents compared to those of Middle Pleistocene Leiqiong feldspars (An=42.1–61.6 mol%; MgO=0.09–0.19 wt%;  $\text{Al}_2\text{O}_3=25.50\text{--}28.76$  wt%;  $\text{Na}_2\text{O}=4.18\text{--}6.38$  wt %; Figure 4). Leiqiong plagioclases have a large variation of An contents (An=40.28–62.20 mol%) including the high-An cores, low-An rims, and intermediate mantle An contents (Figures 5, 6) and show broadly continuous chemical trends (Figure 4). All feldspars show the negative correlations between  $\text{Na}_2\text{O}$ ,  $\text{K}_2\text{O}$ ,  $\text{TiO}_2$ , Ba, La, Eu and An contents (Figures 4A–C, F–H), the positive correlations between MgO,  $\text{Al}_2\text{O}_3$  and An contents (Figures 4D, E).

ZJ-29 (Late Pleistocene) plagioclases show a clear oscillatory zoning texture with irregularly varying incompatible elemental compositions (Figure 5B). ZJ-29 plagioclase groundmass shows significantly higher LREE ( $\text{La}_N=3.62\text{--}14.6$  ppm) and HREE contents ( $\text{Yb}_N=0.05\text{--}0.45$  ppm) and total REE contents ( $\sum\text{REE}_N=16.70\text{--}57.94$  ppm) compared to those of ZJ-29 plagioclase phenocrysts ( $\text{La}_N=3.15\text{--}4.61$  ppm;  $\text{Yb}_N=0.05\text{--}0.16$  ppm;  $\sum\text{REE}_N=15.22\text{--}23.19$  ppm; Figure 5F). ZJ-15, ZJ-43, and ZJ-44

(Middle Pleistocene) plagioclases exhibit complex zoning textures, including a normal zoning texture (ZJ-43 and ZJ-44; Figures 6A, B) and an oscillatory zoning texture (ZJ-15; Figure 5A). ZJ-43 and ZJ-44 plagioclase rims have slightly higher LREE contents ( $\text{La}_N=4.39\text{--}8.91$  ppm;  $\text{La}_N=6.92\text{--}8.13$  ppm) and total REE contents ( $\sum\text{REE}_N=25.08\text{--}46.05$  ppm;  $\sum\text{REE}_N=25.45\text{--}33.49$  ppm) compared to their corresponding plagioclase cores ( $\text{La}_N=3.21\text{--}3.67$  ppm;  $\text{La}_N=6.30\text{--}6.93$  ppm;  $\sum\text{REE}_N=17.33\text{--}23.38$  ppm;  $\sum\text{REE}_N=23.76\text{--}26.16$  ppm; Figures 6E, F). ZJ-15 plagioclase groundmass exhibits relatively higher LREE contents ( $\text{La}_N=5.91\text{--}7.81$  ppm) than those of ZJ-15 plagioclase phenocrysts ( $\text{La}_N=3.22\text{--}4.35$  ppm; Figure 5E). However, ZJ-43 and ZJ-44 plagioclase groundmass have similar or even lower LREE contents compared to their corresponding plagioclase phenocrysts (Figures 6E, F). In addition, all plagioclases display relatively enriched LREE contents ( $\text{La}_N=2.46\text{--}14.6$  ppm), relatively depleted HREE contents ( $\text{Yb}_N=0.01\text{--}0.53$  ppm), slightly large REE differentiation ( $\text{La}/\text{Yb}_N=16.7\text{--}234$ ), and strongly positive Eu anomalies ( $\delta\text{Eu}=6.34\text{--}75.9$ ; Figures 5, 6, Supplementary Figure S7). These plagioclases show the enrichment of Ba, Pb, and Sr relative to Th, Ce, and Nd ( $\text{Ba}/\text{Th}_{\text{PM}}=3.543\text{--}886.0$ ;  $\text{Pb}/\text{Ce}_{\text{PM}}=0.662\text{--}8.447$ ;  $\text{Sr}/\text{Nd}_{\text{PM}}=22.26\text{--}158.1$ ), the negative anomalies of Th, Nb, and Zr relative to U, Ta, and Hf ( $\text{Th}/\text{U}_{\text{PM}}=0.124\text{--}5.371$ ;  $\text{Nb}/\text{Ta}_{\text{PM}}=0.042\text{--}26.47$ ;  $\text{Zr}/\text{Hf}_{\text{PM}}=0.021\text{--}4.676$ ; Figures 5, 6, Supplementary Figure S7).

### 4.4 *In-situ* Sr isotopic compositions of plagioclase

Thirty-three *in-situ* Sr isotopic analyses have been performed on ZJ-15, ZJ-29, ZJ-43, and ZJ-44 plagioclase phenocrysts and groundmass (Figures 5–8; Supplementary Table S6). ZJ-29 (Late Pleistocene) plagioclases exhibit an oscillatory zoning texture with irregular  $^{87}\text{Sr}/^{86}\text{Sr}$  variations. ZJ-29 plagioclase groundmass has significantly higher  $^{87}\text{Sr}/^{86}\text{Sr}$  ratios (0.704,217–0.704543) than those of ZJ-29 plagioclase phenocrysts (0.703706–0.703935; Figure 5D). ZJ-29 bulk-rocks are characterized by much lower

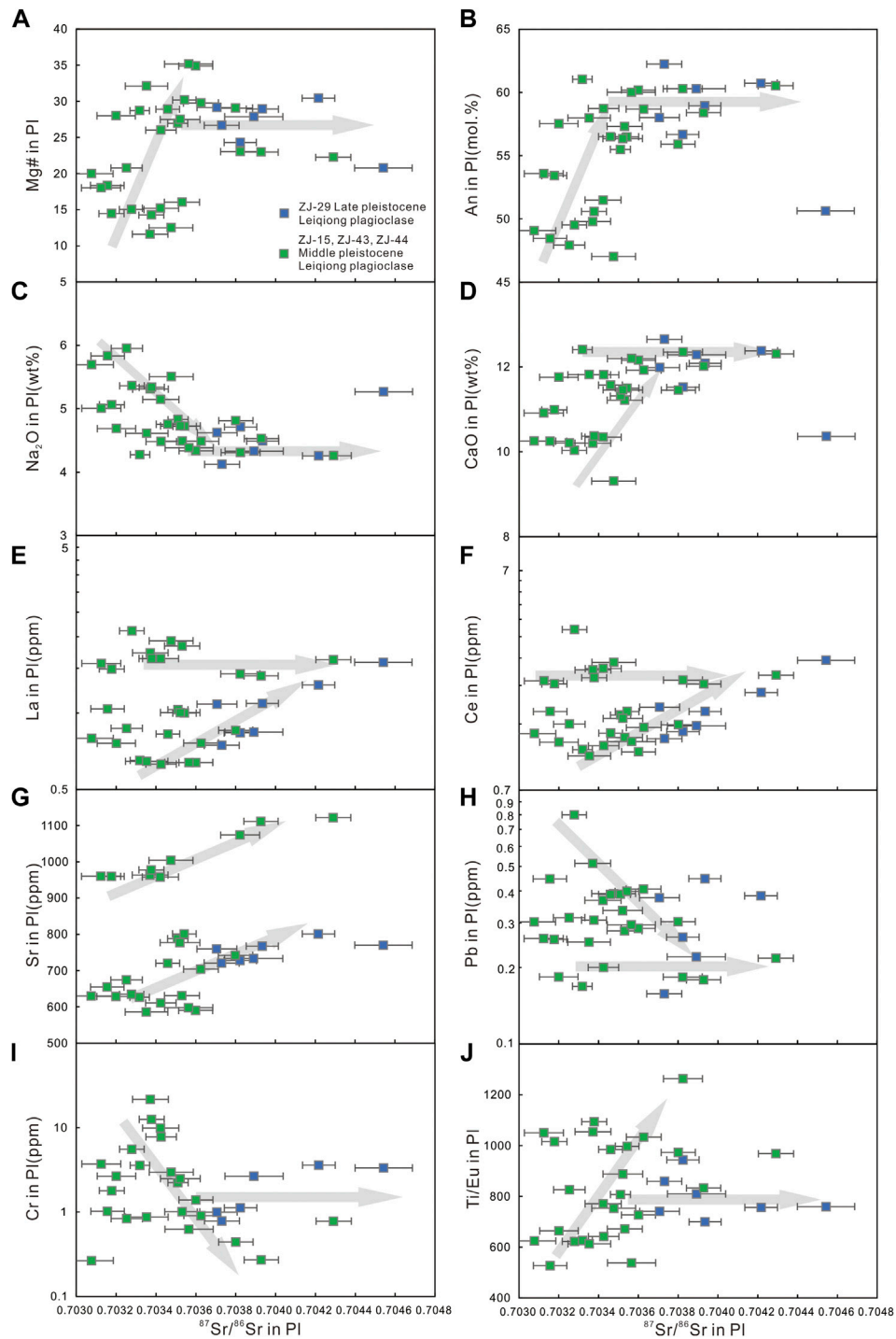
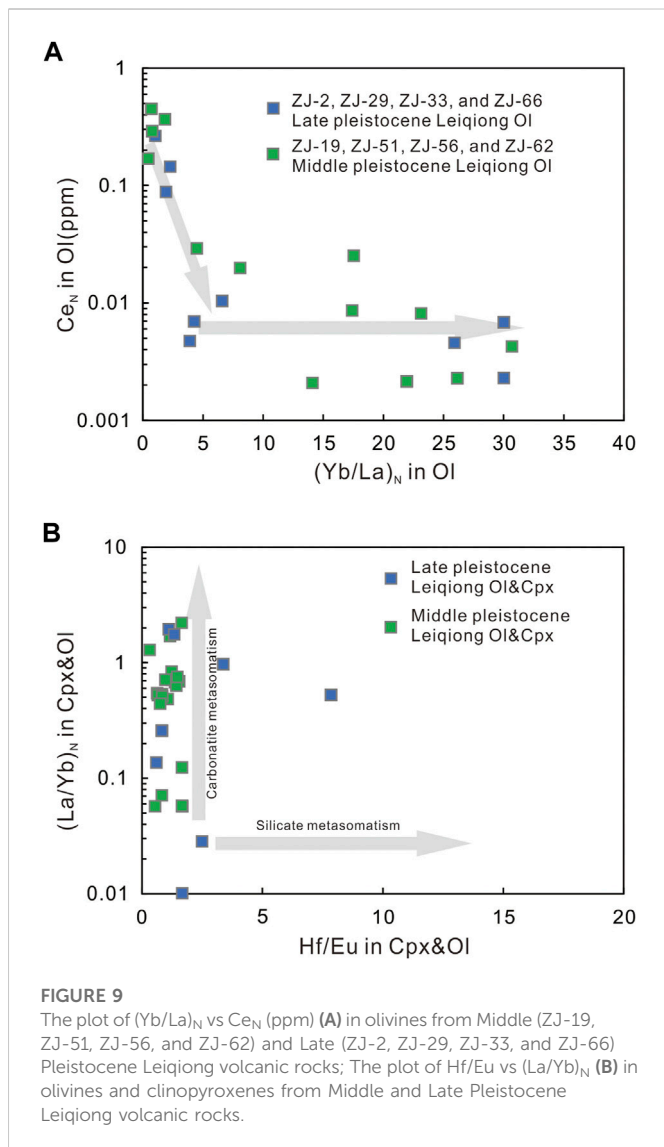


**FIGURE 8**

The plots of  $^{87}\text{Sr}/^{86}\text{Sr}$  vs Mg# (A),  $^{87}\text{Sr}/^{86}\text{Sr}$  vs An (mol%) (B),  $^{87}\text{Sr}/^{86}\text{Sr}$  vs  $\text{Na}_2\text{O}$  (wt%) (C),  $^{87}\text{Sr}/^{86}\text{Sr}$  vs CaO (wt%) (D),  $^{87}\text{Sr}/^{86}\text{Sr}$  vs La (ppm) (E),  $^{87}\text{Sr}/^{86}\text{Sr}$  vs Ce (ppm) (F),  $^{87}\text{Sr}/^{86}\text{Sr}$  vs Sr (ppm) (G),  $^{87}\text{Sr}/^{86}\text{Sr}$  vs Pb (ppm) (H),  $^{87}\text{Sr}/^{86}\text{Sr}$  vs Cr (ppm) (I),  $^{87}\text{Sr}/^{86}\text{Sr}$  vs Ti/Eu (J) for plagioclase phenocrysts and plagioclase groundmass from ZJ-15, ZJ-43, and ZJ-44 (Middle Pleistocene) Leiqiong basalts and ZJ-29 (Late Pleistocene) Leiqiong basalts.

$^{87}\text{Sr}/^{86}\text{Sr}$  ratios (0.703581; Zhu and Wang, 1989) compared to ZJ-29 plagioclase phenocrysts and groundmass (0.703706–0.704543; Figure 7; Supplementary Table S6). ZJ-15, ZJ-43, and ZJ-44 (Middle Pleistocene) plagioclases display a normal (Figures 6A, B) and oscillatory zoning texture (Figure 5A). The variations from relatively higher  $^{87}\text{Sr}/^{86}\text{Sr}$  ratios in the plagioclase rims

(0.703,626–0.703,800; 0.703156–0.703279; 0.703371–0.703476) to relatively lower  $^{87}\text{Sr}/^{86}\text{Sr}$  ratios in their corresponding plagioclase cores (0.703460–0.703543; 0.703077–0.703253; 0.703125–0.703178) are observed from ZJ-15, ZJ-43, and ZJ-44 plagioclase phenocrysts (Figures 5–7; Supplementary Table S6). Nine *in-situ* Sr isotopic ratios were analyzed from ZJ-15, ZJ-43, and ZJ-44 plagioclase groundmass,



displaying relatively higher  $^{87}Sr/^{86}Sr$  ratios (0.703824–0.704291; 0.703319–0.703531; 0.703353–0.703600) than their corresponding plagioclase phenocrysts (0.703460–0.703800; 0.703077–0.703279; 0.703125–0.703476; Figures 5–7; Supplementary Table S6) and bulk-rocks (0.703261; 0.703369; 0.703576; Figure 7; Han et al., 2009; Zhu and Wang, 1989). These Leiqiong plagioclase phenocrysts and groundmass show large Sr isotopic variations from 0.703077 to 0.704543 (Supplementary Table S6), positive correlations between  $^{87}Sr/^{86}Sr$  ratios and Ti/Eu ratio, Mg#, An, CaO, La, Ce, Sr contents, and negative correlations between  $^{87}Sr/^{86}Sr$  ratios and  $Na_2O$ , Pb, Cr contents (Figure 8).

## 5 Discussion

### 5.1 Heterogeneous mantle source

Leiqiong olivine, clinopyroxene, and plagioclase show clear correlation trends (Supplementary Figure S1, S6, Figure 4), likely ascribing to the fractional differentiation of a mantle-derived magma (Zou et al., 2014). Because Rasmussen et al. (2020)

proposed that variations in olivine elemental concentrations with Fo contents (Supplementary Figure S1), elemental variations in plagioclase with An contents (Figure 4), and correlations between clinopyroxene elemental concentrations and Mg# values (Supplementary Figure S6) could effectively evaluate the effects of fractional crystallization, assimilation and diffusion. In addition, ZJ-15 and ZJ-29 Leiqiong plagioclase show an oscillatory zoning texture with significantly variable geochemical and Sr isotopic compositions without remarkably regular patterns (Figures 5A, B). ZJ-43 and ZJ-44 Leiqiong plagioclase show a significantly normal zoning texture with variations from higher Sr isotopic ratios and REE contents in the rims to lower Sr isotopic ratios and REE contents in the cores (Figures 6A, B). ZJ-2, ZJ-29, ZJ-33, and ZJ-66 Leiqiong low-Fo olivine rims display slightly higher REE contents ( $La_N=0.02\text{--}0.17$ ;  $0.01\text{--}0.12$ ;  $0.01\text{--}0.05$ ;  $0.01\text{--}0.16$ ) compared to those of high-Fo olivine cores ( $La_N=0.00\text{--}0.01$ ;  $0.00\text{--}0.01$ ;  $0.00\text{--}0.01$ ;  $0.00\text{--}0.02$ ; Supplementary Figures S2, S3). The intracrystalline Sr isotopic and incompatible element disequilibria within an individual plagioclase and olivine crystal is likely attributed to the contribution to an individual crystal by the incorporation of heterogeneous components during the crystallization of plagioclase, clinopyroxene, and olivine (Lange et al., 2013). Leiqiong plagioclases have large variations of  $^{87}Sr/^{86}Sr$  ratios ranging from 0.703077 to 0.704543 (Figures 5–8) including the high-Sr cores, low-Sr rims, and intermediate mantle  $^{87}Sr/^{86}Sr$  ratios (Figures 5–8). Positive correlations between  $^{87}Sr/^{86}Sr$  ratios and Mg#, An, CaO, La, Ce, Sr, Ti/Eu contents (Figures 8A, B, D–G, J), and negative correlations between  $^{87}Sr/^{86}Sr$  ratios and  $Na_2O$ , Pb, Cr contents (Figure 8C, H–I) are observed, likely further proving the inevitable process of assimilation and fractional crystallization (AFC) (Zou et al., 2014). The assimilation process of different magmatic melts commonly leads to the simultaneous variations in An contents (Pl) and Mg# values (Cpx and Ol) and their corresponding major and trace element and Sr isotope contents (Neave et al., 2013; Zou et al., 2014).

Some Leiqiong olivines have constant  $Ce_N$  contents (0.002–0.009) and variable  $Yb_N/La_N$  ratios (2.364–30.69; Figure 9A), the remaining Leiqiong olivines have a negative correlation between  $Ce_N$  and  $Yb_N/La_N$  with relatively higher  $Ce_N$  contents (0.009–0.449; Figure 9A). This likely further indicates the heterogeneous mantle source compositions (Viccaro et al., 2006; Scarlato et al., 2014; Miller et al., 2017). Because Miller et al. (2017) proposed that the different distribution trends between the cerium contents and HREE/LREE ratios of olivine and clinopyroxene are likely attributed to distinct source compositions (Viccaro et al., 2006; Scarlato et al., 2014).

ZJ-15, ZJ-43, and ZJ-44 (Middle Pleistocene) groundmass plagioclases have much more radiogenic Sr isotopic ratios than their plagioclase phenocrysts and bulk-rocks (Han et al., 2009; Supplementary Table S6; Figure 7). Similarly, ZJ-29 (Late Pleistocene) groundmass plagioclases are distinguished by much higher  $^{87}Sr/^{86}Sr$  ratios than their plagioclase phenocrysts and bulk-rock (Zhu and Wang, 1989; Supplementary Table S6; Figure 7). To sum up, Leiqiong groundmass plagioclases have significantly different  $^{87}Sr/^{86}Sr$  ratios compared to those of their corresponding plagioclase phenocrysts and bulk-rocks (Figure 7). The significant disequilibria of  $^{87}Sr/^{86}Sr$  isotopic

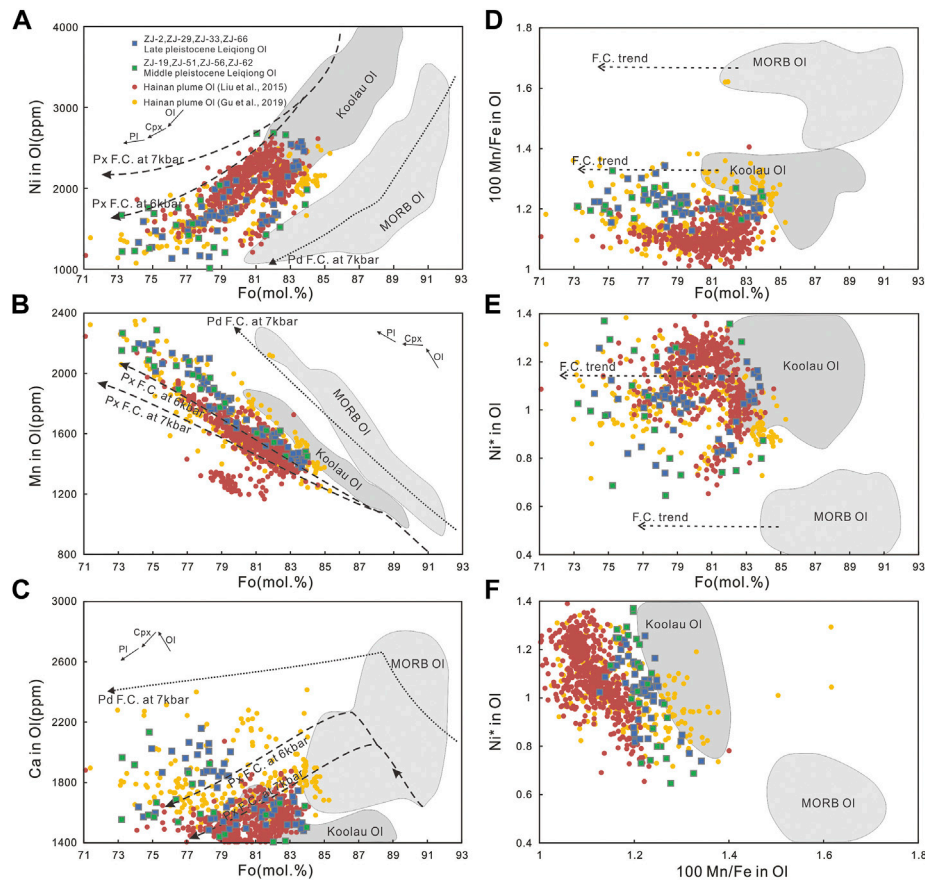


**FIGURE 10**

The plots of Ni (ppm) versus Fo (mol%) (A); Mn (ppm) versus Fo (mol%) (B); Ca (ppm) versus Fo (mol%) (C); 100Mn/Fe versus Fo (mol%) (D); Ni\* versus Fo (mol%) (E); Ni\* versus 100Mn/Fe (F) for Middle (ZJ-19; ZJ-62; ZJ-56; ZJ-51) and Late (ZJ-2; ZJ-29; ZJ-33; ZJ-66) Pleistocene Leiqiong olivines. Ni\* represents Ni/(Mg/Fe)/1,000 ratios. The modelled fractional crystallisation trends from a purely peridotitic (Pd. F.C.) and pyroxenitic (Px. F.C.) are calculated from Danyushevsky and Plechov (2011); Rasmussen et al. (2020). The Koolau (Hawaiian) and MORB olivines are cited from Sobolev et al. (2007).

ratios among bulk-rock, plagioclase phenocryst, and plagioclase groundmass, likely results from an isotopically heterogeneous mantle source (Lange et al., 2013) and a mixture of diverse  $^{87}\text{Sr}/^{86}\text{Sr}$  isotopic compositions from heterogeneous plagioclase (Edwards et al., 2019).

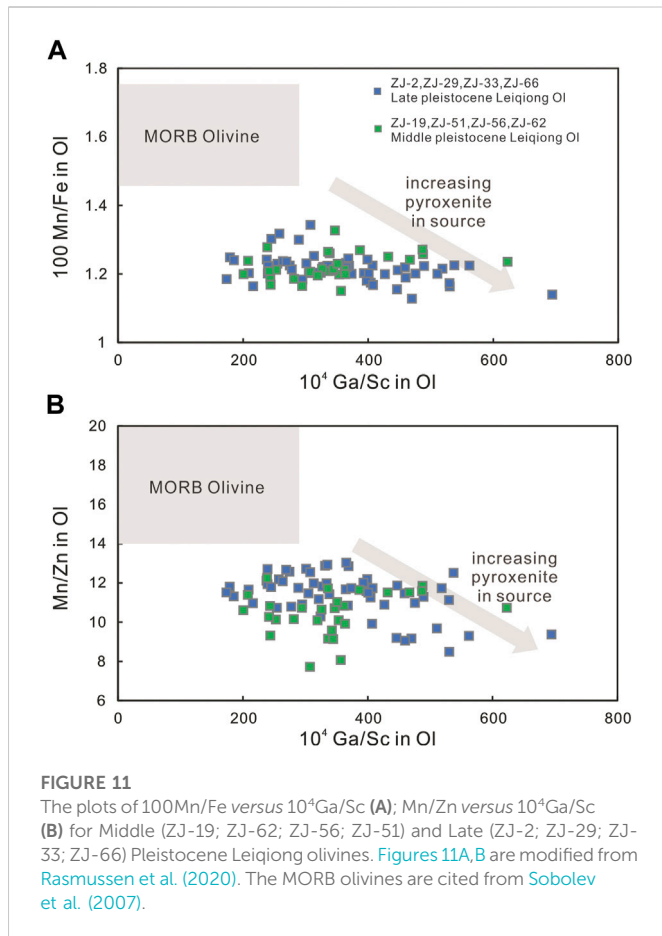
Significant geochemical differences between minerals and hosted bulk-rocks are observed in the Leiqiong volcanic rocks. In detail, ZJ-23, ZJ-40, and ZJ-43 clinopyroxene-equilibrium melts, which are calculated by using the partition coefficients of REE between clinopyroxene and melt (Fig. S8; Hart and Dunn, 1993; Lee et al., 2007), have much higher LREE contents compared to those of their corresponding bulk-rocks (Supplementary Figure S8; Han et al., 2009; Lee et al., 2021). ZJ-15, ZJ-29, ZJ-43, and ZJ-44 plagioclase phenocrysts and groundmass are characterized by much higher and variable  $^{87}\text{Sr}/^{86}\text{Sr}$  ratios relative to those of their corresponding bulk-rocks (Figure 7; Han et al., 2009; Zhu and Wang, 1989). The geochemical disequilibria between minerals and hosted bulk-rocks indicates they are not homologous and/or have suffered from the contamination of geochemically and isotopically heterogeneous mantle source (Zou et al., 2014).

Leiqiong and southern Vietnam Late Cenozoic basaltic rocks exhibit the continuous chemical trends between MgO and  $^{144}\text{Nd}/^{143}\text{Nd}$  and  $^{87}\text{Sr}/^{86}\text{Sr}$ , strongly certifying the AFC processes (An et al.,

2017). Previous SE China bulk-rock Sr-Nd-Pb-Hf isotopic compositions (e.g., Ho et al., 2003; Zou and Fan, 2010; Hoang et al., 2013; An et al., 2017) have also pointed out the isotopically heterogeneous mantle source. Our studied *in-situ* geochemical and isotopic contents within an individual crystal further demonstrated the heterogeneous geochemical compositions at the mineral and sub-mineral scale.

## 5.2 The existence of the hainan plume

ZJ-15, ZJ-29, ZJ-43, and ZJ-44 Leiqiong plagioclases are characterized by the clear enrichment of LREEs and the slight depletion of HREEs, and have similar enriched REE distribution patterns relative to those of Lanai (Hawaiian) plume-type plagioclases (Figures 5, 6; West et al., 1992). ZJ-23, ZJ-40, and ZJ-43 Leiqiong clinopyroxenes display the slight depletion of LREE and HREE, and the negative anomalies of Pb, Sr, and Zr (Figure 3), fully similar to the incompatible element distributions of Snæfellsnes Peninsula (Iceland) plume-type clinopyroxenes (Figure 3; Burney et al., 2020). Leiqiong olivines have remarkably lower Mn (1,375–2,287 ppm) and Ca (1,359–2,157 ppm) contents, lower 100Mn/Fe ratios



(1.127–1.342), and higher  $Ni^*$  ( $Ni/(Mg/Fe)/1,000=0.645\text{--}1.445$ ) and Fe/Mn (74.50–88.72) ratios compared to MORB olivines (Sobolev et al., 2007; Figures 10B–F, S9), similar to those of Koolau (Hawaiian) olivines (Sobolev et al., 2007; Figures 10B–F, S9), Hainan plume olivines (Gu et al., 2019; Liu et al., 2015; Figures 10B–F, S9), and Buðhraun and Berserkjahraun (Iceland) olivines (Kahl et al., 2021; Supplementary Figure S9). It collectively proves that Leiqiong volcanic activities are closely related to a mantle plume. In addition, the calculated Leiqiong clinopyroxene-equilibrium melts show the significantly high LREE contents and slightly depleted HREE contents and display the OIB-type incompatible element pattern (Supplementary Figure S8), suggesting that these Leiqiong volcanic rocks likely origin from the OIB-type plume-type magma. ZJ-15 and ZJ-29 Leiqiong plagioclase groundmass have much higher Sr isotopic ratios (0.703824–0.704291; 0.704217–0.704543) than those of the typical depleted magma (0.702460; Douglass et al., 1999; Zindler and Hart, 1986) and those of the Indian MORB-type magma (0.7026–0.7034; Zindler and Hart, 1986), and have slightly similar Sr isotopic ratios compared to those of the Koolau (Hawaii)-like plume-derived magma (0.7041–0.7045; Lassiter et al., 2000). Thus, ZJ-15 and ZJ-29 plagioclases appear to have crystallized from Koolau-like plume-derived melt. To sum up, the *in-situ* incompatible element and Sr isotopic results of Leiqiong phenocrysts collectively prove the involvement of some plume-related enriched compositions associated with the presence of the Hainan mantle plume.

### 5.3 The pyroxenitic mantle lithology

High-Fo olivines were formed in the early crystallization of primary magma and used to effectively identify the primary mantle source lithology (Rasmussen et al., 2020). Herzberg et al. (2016) has utilized the Ni, Mn, and Ca elemental features of olivines to unravel the olivine-poor and olivine-rich mantle lithologies. The olivine primary magmas have more olivine and less pyroxene phenocrysts, and are therefore characterized by relatively higher Ni contents and relatively lower Ca and Mn contents than those of the olivine derivative magmas (Herzberg, 2011; Søager et al., 2015). Howarth and Harris (2017) proposed that the Zn/Fe, Mn/Zn, and Fe/Mn ratios are sensitive to discriminate the pyroxenite and peridotite source (Le Roux et al., 2011). Fe/Mn ratios are more intensively fractionated in the olivine derivative magmas relative to those of the olivine primary magmas (Qin and Humayun, 2008). Leiqiong olivines show relatively high Fe/Mn (74.5–88.7) ratios, high Ca (1,359–2,157 ppm) and Mn (1,375–2,645 ppm) contents, and low Ni (720–2,684 ppm) contents, mainly plotting within the field of the olivine derivative magmas (Supplementary Figure S9). The above results indicate that Leiqiong olivines are likely crystallized by the incorporation of olivine-poor pyroxenitic mantle source, but different from those from olivine-rich peridotitic mantle lithology.

We took advantage of a forward modelling approach with the Petrolog3 software (Danyushevsky and Plechov, 2011) to estimate the crystal fractionation trend (Figure 10). Sequential crystallisation of olivine, clinopyroxene and plagioclase at 7kbar and 6 kbar from pyroxenite-derived and peridotite-derived source within a simply closed system were carefully investigated (Rasmussen et al., 2020; Figure 10). Model parameters and source compositions are cited from Rasmussen et al. (2020) and Danyushevsky and Plechov (2011). The result shows that our studied Leiqiong olivines are mainly produced by fractional crystallization at the pressure of 6 kbar and/or 7 kbar through a pyroxenite-rich melt-source, but are totally different from those produces derived from a dominantly peridotitic mantle lithology (Figure 10). Rasmussen et al. (2020) exploited the plot of Ga/Sc versus Mn/Zn and Mn/Fe to assess the source lithologies (Howarth and Harris, 2017). Leiqiong olivines have relatively higher  $10^{4*}$ Ga/Sc (173.9–694.4) ratios and lower 100Mn/Fe (1.127–1.342) and Mn/Zn (7.704–13.00) ratios than those of MORB olivines ( $10^{4*}$ Ga/Sc<300; 100Mn/Fe=1.45–1.75; Mn/Zn=14–20; Rasmussen et al., 2020; Sobolev et al., 2007), and plot within the field of the increasing pyroxenite melt (Figure 11), likely indicating they are derived from a dominantly pyroxenitic melt (Søager et al., 2015). In addition, we compared the *in-situ* geochemical compositions of our Leiqiong olivines with Koolau (Hawaii) and typical MORB olivines in Figure 10. The Ni, Mn, and Ca contents, the Mn/Fe and  $Ni^*$  ( $Ni/(Mg/Fe)/1,000$ ) ratios of our studied Leiqiong olivines are partly plotting within the compositional fields of Koolau (Hawaii) olivines, expressing a pyroxenitic melt, but are extremely different from those of MORB olivines, expressing a peridotitic melt source (Figure 10; Sobolev et al., 2007). It suggests the significant involvement of pyroxenite-derived melt in the Leiqiong volcanic activities. During the ascent of the magmatic melt, the partial melting of pyroxenite components generally occurred at higher pressure or greater depths than the melting of peridotitic components (Pertermann and Hirschmann,

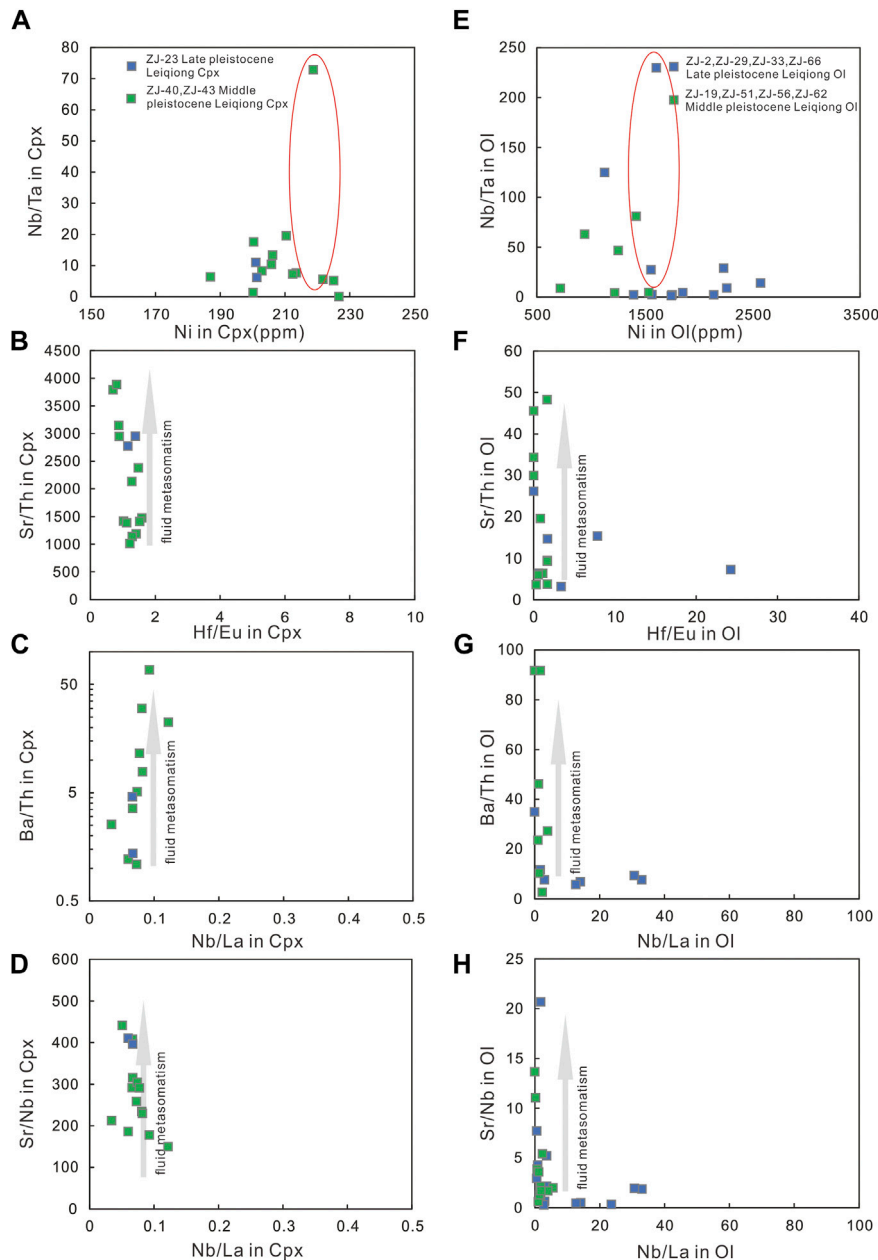


**FIGURE 12**

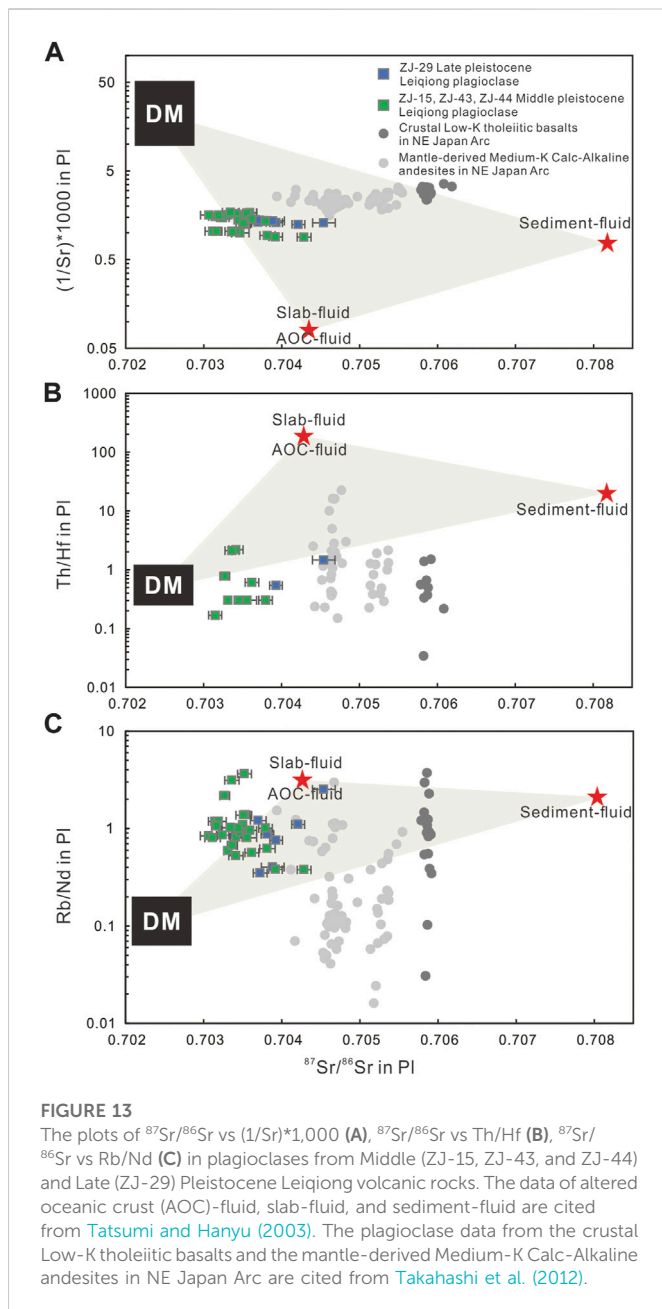
The plots of Ni (ppm) vs Nb/Ta (A), Hf/Eu vs Sr/Th (B), Nb/La vs Ba/Th (C), Nb/La vs Sr/Nb (D) in clinopyroxenes from Middle and Late Pleistocene Leiqiong volcanic rocks. The plots of Ni (ppm) vs Nb/Ta (E), Hf/Eu vs Sr/Th (F), Nb/La vs Ba/Th (G), Nb/La vs Sr/Nb (H) in olivines from Middle and Late Pleistocene Leiqiong volcanic rocks.

2003; Mallik and Dasgupta, 2012). Therefore, the pyroxenitic signal being preserved in the Leiqiong olivines as analyzed above likely indicates their deep-derived signal.

## 5.4 The case for mantle metasomatism due to a paleo-subduction event

The high concentrations of LILE (e.g., Cs, Rb, Ba, Sr) and LREE (e.g., La, Ce, Eu) and the low concentrations of HFSE (e.g., Nb, Ta, Zr, Hf, Th, U) in olivines and clinopyroxenes are commonly interpreted as the signatures of the metasomatism of aqueous

fluid derived from the dehydration of the subducted slab (Dautria et al., 1992; Rudnick et al., 1993; Klemme et al., 1995; Kogiso et al., 1997; Yaxley and Green, 1998; Xu et al., 2013; Zou et al., 2014; Tecchiato et al., 2018; Li et al., 2019; Meshram et al., 2022). Leiqiong olivines and clinopyroxenes show the depletion of Nb and Hf relative to La and Eu ( $Nb/La_{Ol}=0.208-33.08$ ;  $Nb/La_{Cpx}=0.034-0.122$ ;  $Hf/Eu_{Ol}=0.326-24.23$ ;  $Hf/Eu_{Cpx}=0.705-1.594$ ; Figure 12), and the remarkable enrichment of Rb, Ba, and Sr relative to Th and Nb ( $Sr/Th_{Ol}=0.915-3,294$ ;  $Sr/Th_{Cpx}=1,012-3,884$ ;  $Ba/Th_{Ol}=0.817-511.2$ ;  $Ba/Th_{Cpx}=1.090-68.28$ ;  $Sr/Nb_{Ol}=0.106-118.5$ ;  $Sr/Nb_{Cpx}=149.7-441.5$ ; Figure 12), likely suggesting close affinities with the dehydrated aqueous fluid metasomatism (Figure 12; Kogiso



et al., 1997; Xu et al., 2013). Litasov and Ohtani (2010) used experimental petrology to demonstrate that the depletions of HFSE and the large variations of  $(\text{La}/\text{Yb})_{\text{N}}$  (Figure 9B) in olivines and clinopyroxenes may be attributed to the  $\text{CO}_2$ -rich dehydrated fluid metasomatism derived from carbonatite-related subduction. In addition, Leiqiong olivines and clinopyroxenes are distinguished by slightly high Nb/Ta ratios ( $\text{Nb}/\text{Ta}_{\text{O1}}=0.273\text{--}229.7$ ;  $\text{Nb}/\text{Ta}_{\text{Cpx}}=1.330\text{--}72.83$ ) but relatively low Nb ( $\text{Nb}_{\text{O1}}=0\text{--}1.310$  ppm;  $\text{Nb}_{\text{Cpx}}=0.040\text{--}0.154$  ppm) and Ta contents ( $\text{Ta}_{\text{O1}}=0\text{--}0.009$  ppm;  $\text{Ta}_{\text{Cpx}}=0.001\text{--}0.087$  ppm; Figures 12A, E), further confirming the influence of subduction-related exotic fluid metasomatism. This is because rutile can effectively fractionate Nb from Ta and have relatively high Nb/Ta ratios (Klemme et al., 2002). Consequently, the metasomatism of subduction-related fluid/melts inevitably has the involvement of the eclogite with rutile residues, thus leading to

the large variations of Nb/Ta ratios (Kogiso et al., 1997; Klemme et al., 2002).

The formation of a hybrid olivine-free pyroxenitic “fingerprint” is most likely due to the reaction between eclogite-derived silicate melts (recycled oceanic crust) and peridotite (Yaxley and Green, 1998). The contamination of deep recycled oceanic crust and fluid-enriched melts (eclogite pods) from the deep upwelling Hainan plume will likely cause changes in the melt lithology from peridotite to pyroxenite (Yaxley and Green, 1998; Mallik and Dasgupta, 2012).

ZJ-15, ZJ-29, ZJ-43, and ZJ-44 Leiqiong plagioclase rim and groundmass are characterized by clearly more radiogenic Sr isotopic compositions than their plagioclase cores (Figure 7), likely attributing to the assimilation of crustal materials and the involvement of subduction-related fluid. However, An et al., 2017 has basically ruled out the possible role of crustal contamination for the Leiqiong and Vietnamese basaltic rocks. Thus, high *in-situ* Sr isotopic ratios of plagioclase groundmass are mostly attributed to the contamination of subduction-related aqueous fluids, accordingly resulting in the formation of secondary altered minerals in the groundmass (some altered dark-colored mineral particles; Figure 2) and the elevated *in-situ* Rb/Sr ratios, Rb contents, and  $^{87}\text{Sr}/^{86}\text{Sr}$  isotopic signatures of plagioclase groundmass (Ganino et al., 2008; 2013; Karykowski et al., 2017). The interaction between an aqueous fluid and a mafic magma could easily form the clearly high Sr isotopic ratios of plagioclase groundmass and the Sr isotopic disequilibrium between plagioclase phenocrysts and groundmass (Ganino et al., 2008; 2013). In addition, the clear variations of incompatible elements and Sr isotopic compositions of Leiqiong plagioclase phenocrysts from the core to rim are observed (Figures 6C, D). ZJ-43 and ZJ-44 plagioclase rims are characterized by relatively higher  $^{87}\text{Sr}/^{86}\text{Sr}$  isotopic ratios and higher LREE contents than those of plagioclase cores (Figures 6C, D, Figure 7). This intracrystalline Sr isotopic disequilibria within an individual plagioclase likely ascribes to the addition of subduction-related dehydrated fluid metasomatism and the mixture of higher  $^{87}\text{Sr}/^{86}\text{Sr}$  isotopic ratios in the plagioclase rims.

Leiqiong plagioclase phenocrysts and groundmass display large variations of  $^{87}\text{Sr}/^{86}\text{Sr}$  ratios (0.703077–0.704543; Figure 8), positive correlations between  $^{87}\text{Sr}/^{86}\text{Sr}$  and Mg# and Ti/Eu ratios, positive correlations between  $^{87}\text{Sr}/^{86}\text{Sr}$  and An, CaO, La, Ce, Sr concentrations, and negative correlations between  $^{87}\text{Sr}/^{86}\text{Sr}$  and  $\text{Na}_2\text{O}$ , Pb, Cr concentrations (Figure 8), likely suggesting two-endmember magma mixing processes. In addition, Leiqiong plagioclases fall within the mixing lines between sediment-fluid and altered oceanic crust (AOC)/slab-fluid endmember with high  $^{87}\text{Sr}/^{86}\text{Sr}$  ratios (high Th/Hf and Rb/Nd ratios, and low  $(1/\text{Sr}) \times 1,000$  ratios) and depleted mantle endmember with low  $^{87}\text{Sr}/^{86}\text{Sr}$  ratios (low Th/Hf and Rb/Nd ratios, and high  $(1/\text{Sr}) \times 1,000$  ratios) (Figure 13). It further suggests that these Leiqiong volcanic activities are strongly influenced by the subduction-related sediment and fluid.

Our *in-situ* Sr isotopic and geochemical compositions further clearly state the inevitable metasomatism process caused by the deep recycled subduction-related melts from the deep Hainan plume, resulting in the changes in the melt lithology from peridotite to pyroxenite. The deep-derived Hainan plume is likely to carry recycled subduction-related melts/fluids (Hofmann and White, 1982; Sobolev et al., 2007), which reacted with the primary peridotite to form the Leiqiong pyroxenite melt.

## 6 Conclusion

Large amounts of olivine, clinopyroxene, and plagioclase phenocrysts, and plagioclase groundmass from Leiqiong Pleistocene basalts are selected to conduct the *in-situ* major, trace element, and Sr isotope analyses. The micro-trace-element and micro-isotope variations within the individual phenocrysts and groundmass can effectively discuss the mineral-scale magma heterogeneity and the initial mantle-derived features. The normal zoning textures with *in-situ* trace element heterogeneity within an individual Leiqiong olivine, and the complex zoning textures with *in-situ* trace element and  $^{87}\text{Sr}/^{86}\text{Sr}$  isotopic disequilibria within an individual Leiqiong plagioclase likely suggest the contribution to an individual crystal by the incorporation of heterogeneous components. The *in-situ* incompatible element and isotopic compositions of olivine and plagioclase, and the compositions of the calculated Leiqiong clinopyroxene-equilibrium melts show the features of enriched compositions associated with the plume, likely indicating the presence of Hainan mantle plume. The significant disequilibrium of  $^{87}\text{Sr}/^{86}\text{Sr}$  isotopic ratios among bulk-rock, plagioclase phenocryst, and plagioclase groundmass likely indicates the isotopically heterogeneous mantle source and the influence of the recycled subduction-related  $\text{H}_2\text{O}$ -enriched oceanic fluid/melts carried by the deep Hainan plume. Leiqiong olivines are crystallized by the incorporation of pyroxenitic mantle source, but different from those from olivine-rich peridotitic mantle lithology, likely due to the reaction between eclogite-derived silicate melts (recycled oceanic crust) and peridotite.

## Data availability statement

The datasets presented in this study can be found in online repositories. The names of the repository/repositories and accession number(s) can be found in the article/[Supplementary Material](#).

## Author contributions

S-SC and D-YW write and arrange this manuscript. RG and J-QL provide the research funding, propose the research plan, give the

## References

- An, A. R., Choi, S. H., Yu, Y., and Lee, D. C. (2017). Petrogenesis of late cenozoic basaltic rocks from southern Vietnam. *Lithos* 272, 192–204. doi:10.1016/j.lithos.2016.12.008
- Berglund, M., and Wieser, M. E. (2011). Isotopic compositions of the elements 2009 (IUPAC technical report). *Pure Appl. Chem.* 83 (2), 397–410. doi:10.1351/pac-rep-10-06-02
- Brenna, M., Cronin, S. J., Smith, I. E., Maas, R., and Sohn, Y. K. (2012a). How small-volume basaltic magmatic systems develop: A case study from the Jeju island volcanic field, Korea. *J. Petrology* 53, 985–1018. doi:10.1093/petrology/egs007
- Brenna, M., Cronin, S. J., Smith, I. E., Sohn, Y. K., and Maas, R. (2012b). Spatio-temporal evolution of a dispersed magmatic system and its implications for volcano growth, Jeju Island Volcanic Field, Korea. *Lithos* 148, 337–352. doi:10.1016/j.lithos.2012.06.021
- Bryce, J. G., and DePaolo, D. J. (2004). Pb isotopic heterogeneity in basaltic phenocrysts. *Geochimica Cosmochimica Acta* 68, 4453–4468. doi:10.1016/j.gca.2004.01.016
- Burney, D., Peate, D. W., Riisshuus, M. S., and Ukstins, I. A. (2020). Reconstructing the plumbing system of an off-rift primitive alkaline tuya (Vatnafell, Iceland) using geothermobarometry and CSDs. *J. Volcanol. Geotherm. Res.* 399, 106914. doi:10.1016/j.jvolgeores.2020.106914
- Chen, H., Xia, Q. K., Ingrin, J., Delouie, E., and Bi, Y. (2017). Heterogeneous source components of intraplate basalts from NE China induced by the ongoing Pacific slab subduction. *Earth Planet. Sci. Lett.* 459, 208–220. doi:10.1016/j.epsl.2016.11.030
- Chen, L. H., Zeng, G., Jiang, S. Y., Hofmann, A. W., Xu, X. S., and Pan, M. B. (2009). Sources of anfangshan basalts: Subducted lower crust in the sulu UHP belt, China. *Earth Planet. Sci. Lett.* 286, 426–435. doi:10.1016/j.epsl.2009.07.006
- Choi, S. H., Mukasa, S. B., Kwon, S. T., and Andronikov, A. V. (2006). Sr, Nd, Pb and Hf isotopic compositions of late Cenozoic alkali basalts in South Korea: Evidence for mixing between the two dominant asthenospheric mantle domains beneath East Asia. *Chem. Geol.* 232, 134–151. doi:10.1016/j.chemgeo.2006.02.014
- Chung, S. L., Sun, S. S., Tu, K., Chen, C. H., and Lee, C. Y. (1994). Late cenozoic basaltic volcanism around the taiwan strait, SE China: Product of lithosphere-asthenosphere interaction during continental extension. *Chem. Geol.* 112, 1–20. doi:10.1016/0009-2541(94)90101-5
- Danyushevsky, L. V., and Plechov, P. (2011). Petrolog3: Integrated software for modeling crystallization processes. *Geochem. Geophys. Geosystems* 12. doi:10.1029/2011gc003516
- Dautria, J., Dupuy, C., Takherist, D., and Dostal, J. (1992). Carbonate metasomatism in the lithospheric mantle: Peridotitic xenoliths from a melilititic district of the sahara basin. *Contributions Mineralogy Petrology* 111, 37–52. doi:10.1007/bf00296576
- Davidson, J. P., Hora, J. M., Garrison, J. M., and Dungan, M. A. (2005). Crustal forensics in arc magmas. *J. Volcanol. Geotherm. Res.* 140, 157–170. doi:10.1016/j.jvolgeores.2004.07.019
- Dougllass, J., Schilling, J. G., and Fontignie, D. (1999). Plume-ridge interactions of the Discovery and Shona mantle plumes with the southern Mid-Atlantic Ridge (40°–55° S). *J. Geophys. Res. Solid Earth* 104, 2941–2962. doi:10.1029/98jb02642

research ideas, and guide the experimental methods. QC gives a revised opinion.

## Funding

This work was supported by State Key Laboratory of Marine Environmental Science Visiting Fellowship (MELRS2233), Innovation Group Project of Southern Marine Science and Engineering Guangdong Laboratory (Zhuhai) (No.311021003); Guangdong Introducing Innovative and Entrepreneurial Teams; Zhujiang Talent Project Foundation of Guangdong Province (Grant no: 2017ZT07Z066); Fundamental Research Funds for the Central Universities, Sun Yat-sen University (22qntd2101; 2021qntd23); Major Projects of the National Natural Science Foundation of China (41590863); the National Natural Science Foundation of China (42102333; 41806077).

## Conflict of interest

The authors declare that the research was conducted in the absence of any commercial or financial relationships that could be construed as a potential conflict of interest.

## Publisher's note

All claims expressed in this article are solely those of the authors and do not necessarily represent those of their affiliated organizations, or those of the publisher, the editors and the reviewers. Any product that may be evaluated in this article, or claim that may be made by its manufacturer, is not guaranteed or endorsed by the publisher.

## Supplementary material

The Supplementary Material for this article can be found online at: <https://www.frontiersin.org/articles/10.3389/feart.2023.1090803/full#supplementary-material>

- Drouin, M., Godard, M., Ildefonse, B., Bruguier, O., and Garrido, C. J. (2009). Geochemical and petrographic evidence for magmatic impregnation in the oceanic lithosphere at Atlantis Massif, Mid-Atlantic Ridge (IODP Hole U1309D, 30°N). *Chem. Geol.* 264 (1), 71–88. doi:10.1016/j.chemgeo.2009.02.013
- Edwards, M. A., Jackson, M., Kylander-Clark, A., Harvey, J., Hagen-Peter, G., Seward, G., et al. (2019). Extreme enriched and heterogeneous 87Sr/86Sr ratios recorded in magmatic plagioclase from the Samoan hotspot. *Earth Planet. Sci. Lett.* 511, 190–201. doi:10.1016/j.epsl.2019.01.040
- Fan, W., and Menzies, M. (1992). *Geochronology and geochemistry of Cenozoic volcanic rocks in China*. Beijing: Seismic Press, 320–329. The composition of lithospheric mantle in rifting volcanism environment: Geochemical evidence from cenozoic basaltic rocks from Leiqiong area
- Feineman, M., Moriguti, T., Yokoyama, T., Terui, S., and Nakamura, E. (2013). Sediment-enriched adakitic magmas from the Daisen volcanic field, Southwest Japan. *Geochem. Geophys. Geosystems* 14, 3009–3031. doi:10.1002/ggge.20176
- Ganino, C., Arndt, N. T., Zhou, M. F., Gaillard, F., and Chauvel, C. (2008). Interaction of magma with sedimentary wall rock and magnetite ore Genesis in the Panzhihua mafic intrusion, SW China. *Miner. Deposita* 43, 677–694. doi:10.1007/s00126-008-0191-5
- Ganino, C., Harris, C., Arndt, N. T., Prevec, S. A., and Howarth, G. H. (2013). Assimilation of carbonate country rock by the parent magma of the Panzhihua Fe-Ti-V deposit (SW China): Evidence from stable isotopes. *Geosci. Front.* 4, 547–554. doi:10.1016/j.gsf.2012.12.006
- Gao, S., Rudnick, R. L., Carlson, R. W., McDonough, W. F., and Liu, Y. S. (2002). Re–Os evidence for replacement of ancient mantle lithosphere beneath the North China craton. *Earth Planet. Sci. Lett.* 198, 307–322. doi:10.1016/s0012-821x(02)00489-2
- Ge, T., Chen, W., Xu, X., Lee, D., Fan, L., Lee, Q., et al. (1989). The geomagnetic polarity time scale of quaternary for Leiqiong region: The K–Ar dating and palaeomagnetic evidences from igneous rocks. *Chin. J. Geophys.* 32, 550–558.
- Gu, X. Y., Wang, P. Y., Kuritani, T., Hanski, E., Xia, Q. K., and Wang, Q. Y. (2019). Low water content in the mantle source of the Hainan plume as a factor inhibiting the formation of a large igneous province. *Earth Planet. Sci. Lett.* 515, 221–230. doi:10.1016/j.epsl.2019.03.034
- Han, J. W., Xiong, X. L., and Zhu, Z. Y. (2009). Geochemistry of late-cenozoic basalts from Leiqiong area: The origin of EM2 and the contribution from sub-continental lithosphere mantle. *Acta Petrol. Sin.* 25, 3208–3220.
- Hart, S. R., and Dunn, T. (1993). Experimental cpx/melt partitioning of 24 trace elements. *Contributions Mineralogy Petrology* 113, 1–8. doi:10.1007/bf00320827
- Herzberg, C. (2011). Identification of source lithology in the Hawaiian and canary islands: Implications for origins. *J. Petrology* 52, 113–146. doi:10.1093/petrology/egq075
- Herzberg, C., Vidito, C., and Starkey, N. A. (2016). Nickel–cobalt contents of olivine record origins of mantle peridotite and related rocks. *Am. Mineralogist* 101, 1952–1966. doi:10.2138/am-2016-5538
- Ho, K. S., Chen, J. C., and Juang, W. S. (2000). Geochronology and geochemistry of late Cenozoic basalts from the Leiqiong area, southern China. *J. Asian Earth Sci.* 18, 307–324. doi:10.1016/s1367-9120(99)00059-0
- Ho, K. S., Chen, J. C., Lo, C. H., and Zhao, H. L. (2003). 40Ar–39Ar dating and geochemical characteristics of late cenozoic basaltic rocks from the zhejiang–fujian region, SE China: Eruption ages, magma evolution and petrogenesis. *Chem. Geol.* 197, 287–318. doi:10.1016/s0009-2541(02)00399-6
- Hoàng, N., Flower, M. F., Xuàn, P. T., Quý, H. V., Sơn, T. T., and Sơn, T. T. (2013). Collision-induced basalt eruptions at pleiku and buôn mê thuật, south-central Viet Nam. *J. Geodyn.* 69, 65–83. doi:10.1016/j.jog.2012.03.012
- Hofmann, A. W., and White, W. M. (1982). Mantle plumes from ancient oceanic crust. *Earth Planet. Sci. Lett.* 57, 421–436. doi:10.1016/0012-821x(82)90161-3
- Howarth, G. H., and Harris, C. (2017). Discriminating between pyroxenite and peridotite sources for continental flood basalts (CFB) in southern Africa using olivine chemistry. *Earth Planet. Sci. Lett.* 475, 143–151. doi:10.1016/j.epsl.2017.07.043
- Hu, Z., Zhang, W., Liu, Y., Gao, S., Li, M., Zong, K., et al. (2015). Wave” signal-smoothing and mercury-removing device for laser ablation quadrupole and multiple collector ICPMS analysis: Application to lead isotope analysis. *Anal. Chem.* 87 (2), 1152–1157. doi:10.1021/ac503749k
- Huang, J., and Zhao, D. (2006). High-resolution mantle tomography of China and surrounding regions. *J. Geophys. Res. Solid Earth* 111, B09305. doi:10.1029/2005jb004066
- Huang, Z., and Cai, F. (1994). A new approach to the quaternary volcanicity in the Leiqiong area. *Trop. Geogr.* 14, 1–14.
- Jia, Z. B., Chen, H., Xia, Q. K., Liu, J., Zhu, K. Y., Wang, P. Y., et al. (2020). Influence of the subduction of the Pacific plate on the mantle characteristics of South China: Constraints from the temporal geochemical evolution of the Mesozoic basalts in the Jitai Basin. *Lithos* 352, 105253. doi:10.1016/j.lithos.2019.105253
- Jin, Q. Z., Huang, J., Liu, S. C., and Huang, F. (2020). Magnesium and zinc isotope evidence for recycled sediments and oceanic crust in the mantle sources of continental basalts from eastern China. *Lithos* 370, 105627. doi:10.1016/j.lithos.2020.105627
- Kahl, M., Bali, E., Guðfinnsson, G. H., Neave, D. A., Ubide, T., Van Der Meer, Q. H., et al. (2021). Conditions and dynamics of magma storage in the Snæfellsnes volcanic zone, western Iceland: Insights from the búiðhraun and Berserkjahraun eruptions. *J. Petrology* 62, 1–29.
- Karykowski, B. T., Yang, S. H., Maier, W. D., Lahaye, Y., Lissenberg, C. J., and O'Brien, H. (2017). *In situ* Sr isotope compositions of plagioclase from a complete stratigraphic profile of the bushveld complex, south Africa: Evidence for extensive magma mixing and percolation. *J. Petrology* 58, 2285–2308. doi:10.1093/petrology/egy008
- Klemme, S., Blundy, J. D., and Wood, B. J. (2002). Experimental constraints on major and trace element partitioning during partial melting of eclogite. *Geochimica Cosmochimica Acta* 66, 3109–3123. doi:10.1016/s0016-7037(02)00859-1
- Klemme, S. V., Van der Laan, S., Foley, S. F., and Günther, D. (1995). Experimentally determined trace and minor element partitioning between clinopyroxene and carbonatite melt under upper mantle conditions. *Earth Planet. Sci. Lett.* 133, 439–448. doi:10.1016/0012-821x(95)00098-w
- Kogiso, T., Tatsumi, Y., and Nakano, S. (1997). Trace element transport during dehydration processes in the subducted oceanic crust: 1. Experiments and implications for the origin of Ocean Island basalts. *Earth Planet. Sci. Lett.* 148, 193–205. doi:10.1016/s0012-821x(97)00018-6
- Kuritani, T., Ohtani, E., and Kimura, J. I. (2011). Intensive hydration of the mantle transition zone beneath China caused by ancient slab stagnation. *Nat. Geosci.* 4, 713–716. doi:10.1038/ngeo1250
- Lange, A. E., Nielsen, R. L., Tepley, F. J., III, and Kent, A. J. (2013). Diverse Sr isotope signatures preserved in mid-oceanic-ridge basalt plagioclase. *Geology* 41, 279–282. doi:10.1130/g33739.1
- Lassiter, J., Hauri, E., Reiners, P., and Garcia, M. (2000). Generation of Hawaiian post-erosional lavas by melting of a mixed lherzolite/pyroxenite source. *Earth Planet. Sci. Lett.* 178, 269–284. doi:10.1016/s0012-821x(00)00084-4
- Le Roux, V., Dasgupta, R., and Lee, C. T. (2011). Mineralogical heterogeneities in the Earth’s mantle: Constraints from Mn, Co, Ni and Zn partitioning during partial melting. *Earth Planet. Sci. Lett.* 307, 395–408. doi:10.1016/j.epsl.2011.05.014
- Lebedev, S., and Nolet, G. (2003). Upper mantle beneath Southeast Asia from S velocity tomography. *J. Geophys. Res. Solid Earth* 108, doi:10.1029/2000jb000073
- Lee, C. T. A., Harbert, A., and Leeman, W. P. (2007). Extension of lattice strain theory to mineral/mineral rare-earth element partitioning: An approach for assessing disequilibrium and developing internally consistent partition coefficients between olivine, orthopyroxene, clinopyroxene and basaltic melt. *Geochimica Cosmochimica Acta* 71, 481–496. doi:10.1016/j.gca.2006.09.014
- Lee, Y. T., Chou, P. C., Ho, K. S., Tsai, Y. W., and Chang, Y. J. (2021). Petrogenesis of cenozoic basaltic rocks from the Leiqiong area, south China: Evidence from geochemical constraints. *Geochem. Int.* 59, 1199–1234. doi:10.1134/s0016702921130048
- Li, C., and Van Der Hilst, R. D. (2010). Structure of the upper mantle and transition zone beneath Southeast Asia from traveltome tomography. *J. Geophys. Res. Solid Earth* 115, B07308. doi:10.1029/2009jb006882
- Li, W. R., Ji, J. Q., Sang, H. Q., Zhou, J., Tu, J. Y., Sa, X., et al. (2013). Laser 40Ar/39Ar isochron dating on Leizhou Quaternary volcanic rocks. *Acta Petrol. Sin.* 29, 2775–2788.
- Li, X., Zeng, Z., Yang, H., Zhao, Y., Yin, X., Wang, X., et al. (2019). Integrated major and trace element study of clinopyroxene in basic, intermediate and acidic volcanic rocks from the middle Okinawa Trough: Insights into petrogenesis and the influence of subduction component. *Lithos* 352–353, 105320. doi:10.1016/j.lithos.2019.105320
- Li, Y. Q., Kitagawa, H., Nakamura, E., Ma, C., Hu, X., Kobayashi, K., et al. (2020). Various ages of recycled material in the source of cenozoic basalts in SE China: Implications for the role of the hainan plume. *J. Petrology* 61, ega060. doi:10.1093/petrology/egaa060
- Li, Y. Q., Ma, C. Q., and Robinson, P. T. (2016). Petrology and geochemistry of Cenozoic intra-plate basalts in east-central China: Constraints on recycling of an oceanic slab in the source region. *Lithos* 262, 27–43. doi:10.1016/j.lithos.2016.06.012
- Li, Y. Q., Ma, C. Q., Robinson, P. T., Zhou, Q., and Liu, M. L. (2015). Recycling of oceanic crust from a stagnant slab in the mantle transition zone: Evidence from Cenozoic continental basalts in Zhejiang Province, SE China. *Lithos* 230, 146–165. doi:10.1016/j.lithos.2015.05.021
- Litasov, K., and Ohtani, E. (2010). The solidus of carbonated eclogite in the system CaO–Al<sub>2</sub>O<sub>3</sub>–MgO–SiO<sub>2</sub>–Na<sub>2</sub>O–CO<sub>2</sub> to 32 GPa and carbonatite liquid in the deep mantle. *Earth Planet. Sci. Lett.* 295, 115–126. doi:10.1016/j.epsl.2010.03.030
- Liu, J. Q., Ren, Z. Y., Nichols, A. R., Song, M. S., Qian, S. P., Zhang, Y., et al. (2015). Petrogenesis of late cenozoic basalts from north hainan island: Constraints from melt inclusions and their host olivines. *Geochimica Cosmochimica Acta* 152, 89–121. doi:10.1016/j.gca.2014.12.023
- Liu, S. C., Xia, Q. K., Choi, S. H., Delouie, E., Li, P., and Liu, J. (2016). Continuous supply of recycled pacific oceanic materials in the source of cenozoic basalts in SE China: The Zhejiang case. *Contributions Mineralogy Petrology* 171, 100–131. doi:10.1007/s00410-016-1310-4
- Liu, Y., Hu, Z., Gao, S., Günther, D., Xu, J., Gao, C., et al. (2008). *In situ* analysis of major and trace elements of anhydrous minerals by LA-ICP-MS without applying an internal standard. *Chem. Geol.* 257 (1–2), 34–43. doi:10.1016/j.chemgeo.2008.08.004
- Ma, L., Jiang, S. Y., Hofmann, A. W., Dai, B. Z., Hou, M. L., Zhao, K. D., et al. (2014). Lithospheric and asthenospheric sources of lamprophyres in the jiaodong Peninsula: A consequence of rapid lithospheric thinning beneath the North China craton? *Geochimica Cosmochimica Acta* 124, 250–271. doi:10.1016/j.gca.2013.09.035
- Mallik, A., and Dasgupta, R. (2012). Reaction between MORB-eclogite derived melts and fertile peridotite and generation of ocean island basalts. *Earth Planet. Sci. Lett.* 329, 97–108. doi:10.1016/j.epsl.2012.02.007
- Meng, L., Li, Z. X., Chen, H., Li, X. H., and Wang, X. C. (2012). Geochronological and geochemical results from Mesozoic basalts in southern South China Block support the flat-slab subduction model. *Lithos* 132, 127–140. doi:10.1016/j.lithos.2011.11.022
- Meshram, T., Mahapatro, S., Sai, S., Dora, M. L., Randive, K., and Baswani, S. (2022). Petrogenesis of phlogopite-pyroxenite from Southern India: Implications for the link between Proterozoic subduction to rift-related arc magmatism. *Geosystems Geoenvironment* 1, 100033. doi:10.1016/j.geogeo.2022.100033
- Miller, S., Myers, M., Fahnestock, M., Bryce, J., and Blichert-Toft, J. (2017). Magma dynamics of ancient Mt. Etna inferred from clinopyroxene isotopic and trace element systematics. *Geochem. Perspect. Lett.* 4, 47–52. doi:10.7185/geochemlet.1735

- Montelli, R., Nolet, G., Dahlen, F., and Masters, G. (2006). A catalogue of deep mantle plumes: New results from finite-frequency tomography. *Geochem. Geophys. Geosystems* 7. doi:10.1029/2006gc001248
- Morimoto, N. (1988). Nomenclature of pyroxenes. *Mineralogy Petrology* 39, 55–76. doi:10.1007/bf01226262
- Neave, D. A., Passmore, E., MacLennan, J., Fitton, G., and Thordarson, T. (2013). Crystal–melt relationships and the record of deep mixing and crystallization in the ad 1783 Laki Eruption, Iceland. *J. Petrology* 54, 1661–1690. doi:10.1093/petrology/egt027
- Pertermann, M., and Hirschmann, M. M. (2003). Partial melting experiments on a MORB-like pyroxenite between 2 and 3 GPa: Constraints on the presence of pyroxenite in basalt source regions from solidus location and melting rate. *J. Geophys. Res. Solid Earth* 108. doi:10.1029/2000jb000118
- Qin, L., and Humayun, M. (2008). The Fe/Mn ratio in MORB and OIB determined by ICP-MS. *Geochimica Cosmochimica Acta* 72, 1660–1677. doi:10.1016/j.gca.2008.01.012
- Qiu, L., Yan, D. P., Tang, S. L., Chen, F., and Zhang, Y. X. (2019). Cenozoic exhumation of the neoproterozoic sanfang batholith in South China. *J. Geol. Soc.* 177 (2), JGS2019–041.
- Ramos, F. C., and Reid, M. (2005). Distinguishing melting of heterogeneous mantle sources from crustal contamination: Insights from Sr isotopes at the phenocryst scale, Pisgah Crater, California. *J. Petrology* 46, 999–1012. doi:10.1093/petrology/egi008
- Ramos, F. C., Wolff, J. A., and Tollstrup, D. L. (2005). Sr isotope disequilibrium in Columbia River flood basalts: Evidence for rapid shallow-level open-system processes. *Geology* 33, 457–460. doi:10.1130/g21512.1
- Rasmussen, M., Halldórsson, S., Gibson, S., and Guðfinnsson, G. (2020). Olivine chemistry reveals compositional source heterogeneities within a tilted mantle plume beneath Iceland. *Earth Planet. Sci. Lett.* 531, 116008. doi:10.1016/j.epsl.2019.116008
- Ren, Z. Y., Takahashi, E., Orihashi, Y., and Johnson, K. T. (2004). Petrogenesis of tholeiitic lavas from the submarine hana ridge, haleakala volcano, Hawaii. *J. Petrology* 45, 2067–2099. doi:10.1093/petrology/egh048
- Rudnick, R. L., McDonough, W. F., and Chappell, B. W. (1993). Carbonate metasomatism in the northern Tanzanian mantle: Petrographic and geochemical characteristics. *Earth Planet. Sci. Lett.* 114, 463–475. doi:10.1016/0012-821x(93)90076-1
- Scarlato, P., Mollo, S., Blundy, J., Iezzi, G., and Tiepolo, M. (2014). The role of natural solidification paths on REE partitioning between clinopyroxene and melt. *Bull. Volcanol.* 76, 810–814. doi:10.1007/s00445-014-0810-1
- Smith, J. V., and Brown, W. L. (1988). *Nomenclature, general properties of feldspars and simple determinative diagrams, Feldspar Minerals*. Springer, 208–228.
- Soager, N., Portnyagin, M., Hoernle, K., Holm, P. M., Hauff, F., and Garbe-Schönberg, D. (2015). Olivine major and trace element compositions in southern payenia basalts, Argentina: Evidence for pyroxenite–peridotite melt mixing in a back-arc setting. *J. Petrology* 56, 1495–1518. doi:10.1093/petrology/egv043
- Sobolev, A. V., Hofmann, A. W., Kuzmin, D. V., Yaxley, G. M., Arndt, N. T., Chung, S.-L., et al. (2007). The amount of recycled crust in sources of mantle-derived melts. *Science* 316, 412–417. doi:10.1126/science.1138113
- Sun, M., Chen, H., Milan, L. A., Wilde, S. A., Jourdan, F., and Xu, Y. (2018). Continental arc and back-arc migration in Eastern NE China: New constraints on Cretaceous Paleopacific subduction and rollback. *Tectonics* 37, 3893–3915. doi:10.1029/2018tc005170
- Sun, S. S., and McDonough, W. F. (1989). Chemical and isotopic systematics of oceanic basalts: Implications for mantle composition and processes. *Geol. Soc. Lond. Spec. Publ.* 42, 313–345. doi:10.1144/gsl.sp.1989.042.01.19
- Takahashi, T., Hirahara, Y., Miyazaki, T., Senda, R., Chang, Q., Kimura, J. I., et al. (2012). Primary magmas at the volcanic front of the NE Japan arc: Coeval eruption of crustal low-K tholeiitic and mantle-derived medium-K calc-alkaline basalts at azuma volcano. *J. Petrology* 54, 103–148. doi:10.1093/petrology/egs065
- Tang, Y. J., Zhang, H. F., Ying, J. F., Su, B. X., Li, X. H., and Santosh, M. (2013). Rapid eruption of the Ningwu volcanics in eastern China: Response to Cretaceous subduction of the Pacific plate. *Geochem. Geophys. Geosystems* 14, 1703–1721. doi:10.1002/ggge.20121
- Tatsumi, Y., and Hanyu, T. (2003). Geochemical modeling of dehydration and partial melting of subducting lithosphere: Toward a comprehensive understanding of high-Mg andesite formation in the Setouchi volcanic belt, SW Japan. *Geochem. Geophys. Geosystems* 4. doi:10.1029/2003gc000530
- Tecchiato, V., Gaeta, M., Mollo, S., Bachmann, O., Quadt, A. V., and Scarlato, P. (2018). Snapshots of primitive arc magma evolution recorded by clinopyroxene textural and compositional variations: The case of hybrid crystal-rich enclaves from Capo Marargiu Volcanic District (Sardinia, Italy). *Am. Mineralogist* 103 (5–6), 899–910. doi:10.2138/am-2018-6446
- Thompson, R., and Gibson, S. (2000). Transient high temperatures in mantle plume heads inferred from magnesian olivines in Phanerozoic picrites. *Nature* 407, 502–506. doi:10.1038/35035058
- Tu, K., Flower, M. F., Carlson, R. W., Zhang, M., and Xie, G. (1991). Sr, Nd, and Pb isotopic compositions of hainan basalts (south China): Implications for a subcontinental lithosphere dupal source. *Geology* 19, 567–569. doi:10.1130/0091-7613(1991)019<0567:snapic>2.3.co;2
- Viccaro, M., Ferlito, C., Cortesogno, L., Cristofolini, R., and Gaggero, L. (2006). Magma mixing during the 2001 event at mount etna (Italy): Effects on the eruptive dynamics. *J. Volcanol. Geotherm. Res.* 149, 139–159. doi:10.1016/j.jvolgeores.2005.06.004
- Wang, S., and Zhang, G. L. (2022). Geochemical constraints on mantle source nature and recycling of subducted sediments in the Sulu Sea. *Geosystems Geoenvironment* 1, 100005. doi:10.1016/j.geogeo.2021.10.001
- Wang, X. C., Li, Z. X., Li, X. H., Li, J., Liu, Y., Long, W. G., et al. (2012). Temperature, pressure, and composition of the mantle source region of late cenozoic basalts in hainan island, SE Asia: A consequence of a young thermal mantle plume close to subduction zones? *J. Petrology* 53, 177–233. doi:10.1093/petrology/egr061
- Wei, S. S., and Chen, Y. J. (2016). Seismic evidence of the Hainan mantle plume by receiver function analysis in southern China. *Geophys. Res. Lett.* 43, 8978–8985. doi:10.1002/2016gl069513
- West, H., Garcia, M., Gerlach, D., and Romano, J. (1992). Geochemistry of tholeiites from Lanai, Hawaii. *Contributions Mineralogy Petrology* 112, 520–542. doi:10.1007/bf00310782
- Xu, W. L., Zhou, Q. J., Pei, F. P., Yang, D. B., Gao, S., Li, Q. L., et al. (2013). Destruction of the North China craton: Delamination or thermal/chemical erosion? Mineral chemistry and oxygen isotope insights from websterite xenoliths. *Gondwana Res.* 23, 119–129. doi:10.1016/j.jgr.2012.02.008
- Xu, Y. G. (2001). Thermo-tectonic destruction of the archaean lithospheric keel beneath the sino-Korean craton in China: Evidence, timing and mechanism. *Phys. Chem. Earth, Part A Solid Earth Geodesy* 26, 747–757. doi:10.1016/s1464-1895(01)00124-7
- Xu, Y., Li, H., Hong, L., Ma, L., Ma, Q., and Sun, M. (2018). Generation of Cenozoic intraplate basalts in the big mantle wedge under eastern Asia. *Sci. China Earth Sci.* 61, 869–886. doi:10.1007/s11430-017-9192-y
- Yan, Q., Shi, X., Metcalfe, I., Liu, S., Xu, T., Kornkanitnan, N., et al. (2018). Hainan mantle plume produced late Cenozoic basaltic rocks in Thailand, Southeast Asia. *Sci. Rep.* 8, 6299–6328. doi:10.1038/s41598-018-20712-7
- Yaxley, G. M., and Green, D. H. (1998). Reactions between eclogite and peridotite: Mantle refertilisation by subduction of oceanic crust. *Schweiz. Mineral. Petrogr. Mittl.* 78, 243–255.
- Yu, J. H., O'Reilly, S. Y., Griffin, W., Xu, X., Zhang, M., and Zhou, X. (2003). The thermal state and composition of the lithospheric mantle beneath the Leizhou Peninsula, South China. *J. Volcanol. Geotherm. Res.* 122, 165–189. doi:10.1016/s0377-0273(02)00500-0
- Yu, M., Yan, Y., Huang, C. Y., Zhang, X., Tian, Z., Chen, W. H., et al. (2018). Opening of the South China Sea and upwelling of the hainan plume. *Geophys. Res. Lett.* 45, 2600–2609. doi:10.1002/2017GL076872
- Yu, X., Zeng, G., Chen, L. H., Wang, X. J., Liu, J. Q., Xie, L. W., et al. (2019). Evidence for rutile-bearing eclogite in the mantle sources of the Cenozoic Zhejiang basalts, eastern China. *Lithos* 324, 152–164. doi:10.1016/j.lithos.2018.11.003
- Zeng, G., He, Z. Y., Li, Z., Xu, X. S., and Chen, L. H. (2016). Geodynamics of paleo-Pacific plate subduction constrained by the source lithologies of Late Mesozoic basalts in southeastern China. *Geophys. Res. Lett.* 43 (10), 10,189197–10,197. doi:10.1002/2016gl070346
- Zhang, G. L., Luo, Q., Zhao, J., Jackson, M. G., Guo, L. S., and Zhong, L. F. (2018). Geochemical nature of sub-ridge mantle and opening dynamics of the South China Sea. *Earth Planet. Sci. Lett.* 489, 145–155. doi:10.1016/j.epsl.2018.02.040
- Zhang, J. J., Zheng, Y. F., and Zhao, Z. F. (2009). Geochemical evidence for interaction between oceanic crust and lithospheric mantle in the origin of Cenozoic continental basalts in east-central China. *Lithos* 110, 305–326. doi:10.1016/j.lithos.2009.01.006
- Zhang, M., and Guo, Z. (2016). Origin of Late Cenozoic Abaga–Dalinoer basalts, eastern China: Implications for a mixed pyroxenite–peridotite source related with deep subduction of the Pacific slab. *Gondwana Res.* 37, 130–151. doi:10.1016/j.jgr.2016.05.014
- Zhang, W., Hu, Z., and Liu, Y. (2020). Iso-compass: New freeware software for isotopic data reduction of LA-MC-ICP-MS. *J. Anal. Atomic Spectrom.* 35 (6), 1087–1096. doi:10.1039/d0ja00084a
- Zhang, W., Hu, Z., Liu, Y., Wu, T., Deng, X., Guo, J., et al. (2018). Improved *in situ* Sr isotopic analysis by a 257 nm femtosecond laser in combination with the addition of nitrogen for geological minerals. *Chem. Geol.* 479, 10–21. doi:10.1016/j.chemgeo.2017.12.018
- Zhou, P., and Mukasa, S. B. (1997). Nd–Sr–Pb isotopic, and major-and trace-element geochemistry of cenozoic lavas from the khorat plateau, Thailand: Sources and petrogenesis. *Chem. Geol.* 137, 175–193. doi:10.1016/s0009-2541(96)00162-3
- Zhou, X. H., Zhu, B. Q., Liu, R. X., and Chen, W. J. (1988). *Cenozoic basaltic rocks in eastern China, Continental flood basalts*. Springer, 311–330.
- Zhu, B., and Wang, H. (1989). Nd–Sr–Pb isotopic and chemical evidence for the volcanism with MORB–OIB source characteristics in the Leiqiong area, China. *Geochimica* 3, 193–201.
- Zindler, A., and Hart, S. (1986). Chemical geodynamics. *Annu. Rev. earth Planet. Sci.* 14, 493–571. doi:10.1146/annurev.ea.14.050186.002425
- Zong, K., Klemd, R., Yuan, Y., He, Z., Guo, J., Shi, X., et al. (2017). The assembly of Rodinia: The correlation of early Neoproterozoic (ca. 900 Ma) high-grade metamorphism and continental arc formation in the southern Beishan Orogen, southern Central Asian Orogenic Belt (CAOB). *Precambrian Res.* 290, 32–48. doi:10.1016/j.precamres.2016.12.010
- Zou, D., Liu, Y., Hu, Z., Gao, S., Zong, K., Xu, R., et al. (2014). Pyroxenite and peridotite xenoliths from Hexigten, Inner Mongolia: Insights into the Paleo-Asian Ocean subduction-related melt/fluid–peridotite interaction. *Geochimica Cosmochimica Acta* 140, 435–454. doi:10.1016/j.gca.2014.05.046
- Zou, H., and Fan, Q. (2010). U–Th isotopes in Hainan basalts: Implications for sub-asthenospheric origin of EM2 mantle endmember and the dynamics of melting beneath Hainan Island. *Lithos* 116, 145–152. doi:10.1016/j.lithos.2010.01.010
- Zou, H., Zindler, A., Xu, X., and Qi, Q. (2000). Major, trace element, and Nd, Sr and Pb isotope studies of cenozoic basalts in SE China: Mantle sources, regional variations, and tectonic significance. *Chem. Geol.* 171, 33–47. doi:10.1016/s0009-2541(00)00243-6